NEUTRON ATYPICAL EFFECTS AND THE INFLUENCE ON THE RADIATION RESPONSE OF METALLIC ALLOYS AT ULTRA-HIGH DAMAGE LEVELS

A Dissertation

by

JONATHAN G. GIGAX

Submitted to the Office of Graduate and Professional Studies of
Texas A&M University
in partial fulfillment of the requirements for the degree of

DOCTOR OF PHILOSOPHY

Chair of Committee,	Lin Shao
Committee Members,	Karl Hartwig
	Craig Marianno
	Sean McDeavitt
Head of Department,	Yassin A. Hassan

December 2017

Major Subject: Nuclear Engineering

ABSTRACT

Cladding materials in next-generation fast reactors are expected to reach damage levels of 500 displacements per atom (dpa) or greater during the lifetime of the fuel. Austenitic stainless steel cladding showed excessive void swelling that limited the lifetime of the fuel, ultimately reducing the fuel economy. Ferritic-martensitic steels have been shown to be more resistant to void swelling than their austenitic counterparts, swelling at a rate of 0.2%/dpa compared to 1%/dpa in the steady-state swelling regime. With few fast flux facilities capable of achieving 500 displacements per atom within a few decades, ion irradiation has been selected as a surrogate for neutron irradiation to quickly screen fuel cladding candidates.

Ion irradiation, however, differs intrinsically from neutron irradiation and several of these differences dramatically impact the microstructural development under irradiation. Before engaging in ultra-high damage level irradiations, an understanding of these neutron atypical phenomena is required. In this work, three of the neutron atypical effects that influence the radiation response most strongly are investigated: defect imbalance, temporal damage rate gradients, and compositional modification by Coulomb drag induced via ion bombardment. Although the defect imbalance effect is intrinsic to ion irradiation, using a static defocused beam and a specialized filtering system can reduce the effect that the latter two neutron atypical phenomena have on the microstructural development.

At low damage levels (<100 dpa), structural engineering to produce fine-grained microstructures resulted superior radiation resistance. There are no studies that have examined the response at high damage levels in order to determine the stability of the microstructure. A ferritic/martensitic alloy, T91, and its variant subject to equal channel angular extrusion are irradiated to 1000 dpa and the radiation response of microstructures compared in order to evaluate the stability of features produced by severe deformation at damage levels expected in next-generation fast reactors.

DEDICATION

For my family, friends, and mentors who have guided and encouraged me in my studies.

CONTRIBUTORS AND FUNDING SOURCES

This study was supervised by a dissertation committee consisting of Professor Lin Shao (advisor), Professor Craig M. Marianno, and Professor Sean M. Mcdeavitt of the department of Nuclear Engineering, and Professor Karl T. Hartwig of the department of material science and engineering.

Professor Lin Shao provided the modelling data and analysis for the study in chapter 2. Cao-Chen Wei, Assel Aitkaliyeva, Di Chen, Buelent H. Sencer, and Frank A. Garner contributed to the writing and editing of the manuscript.

The specimen preparation for the study in chapter 3 was assisted by Eda Aydogan. Yuedong Wu, Wei-Yang Lo, and Professor Yong Yang helped prepare specimens for microscopy and editing for the manuscript. Tianyi Chen performed microscopy on the irradiated specimens. Professor Lin Shao, Frank Garner, and Di Chen assisted in editing and providing critical review of the manuscript.

Specimen preparation for ion irradiation was performed by Eda Aydogan for the study in chapter 4. Hyosim Kim prepared microscopy specimens of the irradiated samples and assisted in the irradiation. Stu Maloy provided the bulk material and editing of the manuscript. Professor Lin Shao and Frank Garner provided assistance with analysis of specimen composition and editing of the published manuscript.

For the study in chapter 5, Tianyi Chen and Hyosim Kim both helped prepare microscopy specimens and performed microscopy on the irradiated specimens. Lloyd M. Price assisted with the irradiation of the specimens. Jing Wan, Dan K. Schreiber, and Mychailo Toloczko performed some microscopy (atom-probe tomography) and analysis of the irradiated specimens. Professor Lin Shao, Frank Garner, Eda Aydogan, and Stu Maloy all contributed to the writing and editing of the manuscript.

Hyosim Kim and Tianyi Chen assisted in specimen preparation for microscopy in the study detailed in chapter 6. Professor Lin Shao and Frank Garner both provided extensive guidance for the analysis of the data and editing of the published manuscript.

All other work conducted for the dissertation was completed by the student.

These studies were made possible in part by the National Science Foundation through grant CMMI-0846835, by U.S. Department of Energy, NEUP program, through grant DE-NE0008297, and by the U.S. Department of Energy, through DOE-NE Operations Office Contract DE-AC07-051D14517.

TABLE OF CONTENTS

Page

LIST OF FIGURES

LIST OF TABLES

1. INTRODUCTION*

For advanced nuclear reactor concepts, there is a critical need for structural materials that can withstand radiation damage levels that are much higher than can be reached by currently used austenitic steels. In the 1970s to 1990s there were a number of national alloy development programs for liquid metal reactors that worked to extend the swelling resistance of austenitic alloys for fast reactor concepts. All programs

---

*A part of this chapter is reprinted with permission from "Effect of defect imbalance on void swelling distributions produced in pure iron by 3.5 MeV self-ions", Lin Shao, Cao-Chen Wei, Jonathan G. Gigax, Assel Aitkaliyeva, Di Chen, Buelent H. Sencer, Frank A. Garner, Journal of Nuclear Materials 453 (2014) pp. 176-181, Copyright 2017 by Elsevier.

A part of this chapter is reprinted with permission from "The influence of ion beam rastering on the swelling of self-ion irradiated pure iron at 450°C", Jonathan G. Gigax, Eda Aydogan, Tianyi Chen, Di Chen, Lin Shao, Yuedong Wu, Wei-Yang Lo, Yong Yang, Frank A. Garner, Journal of Nuclear Materials 465 (2015) pp. 343-348, Copyright 2017 by Elsevier.

A part of this chapter is reprinted with permission from "Beam-contamination-induced compositional alteration and its neutron-atypical consequences in ion simulation of neutron-induced void swelling", Jonathan G. Gigax, Hyosim Kim, Eda Aydogan, Stuart A. Maloy, Frank A. Garner, and Lin Shao, Material Research Letters (2017) pp. 1-8, available online at http://dx.doi.org/10.1080/21663831.2017.1323808. Published by Informa UK Limited, trading as Taylor & Francis Group under Creative Commons Attribution License (http://creativecommons.org/licenses/by/4.0/).

A part of this chapter is reprinted with permission from "Radiation response of alloy T91 at damage levels up to 1000 peak dpa", Jonathan G. Gigax, Tianyi Chen, Hyosim Kim, Jing Wang, Lloyd M. Price, Eda Aydogan, Stuart A. Maloy, Dan K. Schreiber, Mychailo Toloczko, Frank A. Garner, and Lin Shao, Journal of Nuclear Materials 482 (2016) pp. 257-265, Copyright 2017 by Elsevier.

A part of this chapter is reprinted with permission from "Radiation instability of equal channel angular extruded T91 at ultra-high damage levels", Jonathan G. Gigax, Hyosim Kim, Tianyi Chen, Frank A. Garner, and Lin Shao, Acta Materialia 132 (2017) pp. 395-404, Copyright 2017 by Elsevier.

eventually focused on the use of titanium-modified austenitic steels based on 316 stainless with higher nickel levels, optimized minor element compositions, and improved fabrication procedures for use as fuel cladding and structural components [1,2]. It had been determined earlier, however, that these modified alloys and all austenitic steels would eventually swell at ~1%/dpa at all reactor-relevant temperatures after some incubation dose, with the largest observed incubation delay in the range of 100-150 dpa. It was also observed that alloy optimization would only delay, but not preclude the eventual onset of this higher swelling regime [3-6].

Additionally, it was learned that at ~10% void swelling, austenitic stainless steels developed a new form of severe void-induced embrittlement that became the life-limiting condition for its use as fuel cladding [7-9]. A consequence of this embrittlement was a limitation on fuel burn-up to 10-12%, far short of the ~30% burn-up limitation imposed by fission product accumulation, thereby strongly impacting the economics of power generation in fast reactors. In effect, the economics of power production were dictated by the cladding and not by the much more expensive fuel. To reach optimum higher burn-ups approaching 30% requires materials to be able to withstand 250-350 dpa, depending on the reactor flux-spectra, while some other reactor concepts such as "traveling wave" or actinide "burners" envision doses as high as 400-600 dpa.

It is recognized that one possible solution is to use ferritic or ferritic/martensitic alloys (F/M) which have been shown to swell much less than austenitic alloys during neutron irradiation [10]. In fact, simple body-centered cubic (bcc) iron-based alloys have longer swelling incubation periods and a lower swelling per dpa rate (~0.2%/dpa) in the steady-state void growth region than do simple face-centered cubic (fcc) iron-based alloys (~1.0%/dpa) [10,11]. It was also observed that several commercial F/M alloys (HT9 and 9Cr-1Mo) also swelled at ~0.2%/dpa at very high neutron-induced dpa levels of 100-200 dpa.

Odette suggested a number of factors that produce the superior swelling resistance of F/M alloys compared to austenitic alloys [12]. The first proposed mechanism is that the more open bcc lattice results in a lower interstitial bias to

dislocations, leading to a lower vacancy population. Additionally, the bcc lattice exists at a higher homologous temperature than the face centered cubic (fcc) lattice, reducing the vacancy supersaturation level that drives void nucleation. Another mechanism postulated by Sniegowski and Wolfer argued the differences in formation and migration energies of vacancies and interstitials in the fcc and bcc iron-base systems might account for the differences in post-transient swelling rate [13]. Most interestingly, before experimental data were available, Sniegowski and Wolfer correctly predicted that bcc iron-base alloys would swell at a lower rate of ~0.2%/dpa compared to the ~1%/dpa characteristic of fcc iron-based alloys.

Other factors have been proposed to account for the lower swelling rate of bcc iron-base alloys. Two prominent types of dislocation loops are observed in bcc iron systems consisting of a<100> and a/2<111> loops. Since a<100> dislocation loops are stronger interstitial sinks compared to a/2<111> loops, which are neutral sinks for both interstitial and vacancy defects, the bias of interstitials to a<100> loops results in a larger removal of vacancies by the more dominant a/2<111> loops [14,15]. The unfaulting of sessile loops and dislocation mobility is also thought to strongly influence swelling behavior. High swelling rates in the transient swelling regime are characterized by the movement of dislocation loops and formation of a complex dislocation network, with steady-state swelling observed afterwards. All of these factors have been proposed as mechanisms that contribute to the swelling resistance under both ion and neutron irradiation.

Second, variations in minor solute concentrations have been observed to influence swelling in bcc iron-base alloys. Experimental studies have shown a strong effect of Cr concentration, with some suggesting that defect trapping by Cr atoms promotes defect recombination and strongly influenced subsequent swelling with the maximum suppression around 12 wt% Cr [16-19]. Minor solute elements, such as Si, Mo, Nb, V, Mn, Ni and C, are also observed to play a role in trapping point defects by producing solute-defect systems that enhance defect recombination [16,19].

In addition to alloying engineering, structural engineering through severe deformation has been a subject of great interest to improve radiation tolerance by formation of dense grain boundaries [21]. In particular, equal channel angular extrusion (ECAE) has been applied to complex alloys to introduce large strains in a material without a reduction in specimen size, offering a possibility for producing a fine grain structure [22-24]. Alloy processing by ECAE results in a large increase in dislocation and grain boundary density. Grain boundaries are efficient sinks for interstitials, vacancies, and gas atoms, and have been shown to effectively suppress swelling in some studies [25,26]. A previous low damage level study of T91 refined by ECAE has shown the processed material to possess superior radiation resistance compared to an unrefined T91 specimen [27]. However, the damage level achieved in that study was far below the 200-600 dpa required in next-generation reactor concepts. Furthermore, neither specimen with and without grain refinement exhibited the 0.2%/dpa steady-state swelling rate observed in neutron irradiated Fe-Cr alloys [28]. From the previous data, it is difficult to evaluate the impact of ECAE-induced grain refinement on radiation resistance at higher reactor-relevant doses.

The concern stems from the radiation instability of fine grain structures. In both thin film and bulk nanocrystalline specimens, grain growth has been reported to occur under irradiation [29-32]. At present, the influence of a growing grain boundary on the defect population is currently unknown. The limited information on the high damage level response naturally raises the question: How do optimized alloys and their structurally engineered counterparts behave at high damage levels?

The solution, it would seem, is to simply irradiate these alloys to high damage levels to understand the microstructural evolution. Neutron irradiation is the preferred choice. However, the limited availability of facilities with sufficiently high fast flux to reach damage levels in excess of 500 dpa renders this choice unsuitable for studying the wide range of variations on a single alloy, much less several alloys and their variants. The best alternative to neutron irradiation has been the subject of debate for many decades, with heavy ion irradiation being accepted as a suitable surrogate and

successfully employed as tool for studying the radiation response of a wide range of materials.

The purpose of this work is not to validate the use of ion irradiation as a tool to simulate neutron irradiation. Rather, effort is invested into understanding the limitations of the tool and applying it to study the radiation stability at damage levels previously unachieved. The significance of this work can be understood from the two main objectives. First, while many acknowledge one or two of the phenomena that arise uniquely in ion irradiation, termed neutron atypical effects, very few are aware of or acknowledge the impact these effects have on the microstructural evolution when all are operating synergistically. In order to utilize ion irradiation to effectively simulate neutron damage, understanding neutron atypical phenomena and the influence these have on the microstructural development is paramount. Three neutron atypical effects are explored:

1) The impact of the spatial heterogeneity of defects arising from ion interactions on the microstructure is examined.
2) The differences between a pulsed and steady-state beam on the defect evolution are studied.
3) A previously unreported phenomenon involving the influence of contaminants injected via Coulomb-drag effects on void swelling and radiation-induced precipitation is investigated.

It is important to acknowledge that there are other neutron atypical effects not presented in this work. The studied effects, however, are among those that impact microstructural evolution most strongly. By identifying and understanding the impact these neutron atypical effects have on the microstructural development of ion irradiated alloys, a standard or procedure can be developed to minimize the influence of these effects.

Second, many conclusions on the radiation resistance of engineered materials have been formed at low damage levels. Although the validity of the results within the low damage level regime is not debated, the relevance to high damage levels is

questionable. The second objective of this work is to utilize heavy ion irradiation, guided by the developed procedure and understanding of neutron atypical effects, to study the radiation response of a F/M alloy, T91, and evaluate the radiation stability of its structurally engineering variant to ultra-high damage levels. A study to investigate the stability of oxide dispersion strengthened alloys at high damage levels is currently ongoing.

2. DEFECT IMBALANCE PHENOMENON*

When performing ion irradiation studies, there are generally two categories of ions for consideration. Light ions, typically protons and helium ions, with energies of several MeV are widely employed due to their deep penetration depth and relatively flat damage profile in the near surface region. These qualities are ideal for studying radiation effects on structures that span several micrometers in length (e.g. grain boundaries). Due to their relatively strong Coulombic interactions, the heat generation per dpa limits the maximum damage rate that can be used to avoid overheating the specimen [33]. Thus, to achieve high damage levels via light ions requires careful control over long periods of time and is generally avoided.

Heavy ions, however, have much shallower penetration depths with a much larger variation in dpa rate over the ion range. However, the defect population produced by heavy ions are more similar to those produced by neutrons [33,34]. Furthermore, the lower heat generation rate enables the use of high dpa rates to achieve 100s of dpa in the span of a few days. There are a number of neutron atypical processes that must be considered when performing heavy ion irradiations. These include the effects from the influence of the surface (e.g. sputtering) and defect imbalances arising from forward scattering and the injected interstitial [35]. There are also effects from the large internal

*Reprinted with permission from "Effect of defect imbalance on void swelling distributions produced in pure iron by 3.5 MeV self-ions", Lin Shao, Cao-Chen Wei, Jonathan G. Gigax, Assel Aitkaliyeva, Di Chen, Buelent H. Sencer, Frank A. Garner, Journal of Nuclear Materials 453 (2014) pp. 176-181, Copyright 2017 by Elsevier.

dpa rate gradient, ion beam rastering, segregation along dpa gradients, and lack of concurrent hydrogen and helium generation [36-40]. Before examining the other neutron atypical effects, the primary effect (i.e. defect imbalance) will be examined first in this section.

The defect imbalance effect is the spatial difference in interstitial and vacancy distributions caused by forward scattering (interstitials distributed deeper than vacancies) and the implanted ion (injected interstitial). It is important to note that both correlated (defects created from knock-on collisions) and uncorrelated collisions (defects from different damage cascades or collision events) contribute to the defect imbalance effect. When examining the role of the defect imbalance effect, a model is proposed to calculate the zero-time point defect distributions. Since point defects are difficult to see in conventional transmission electron microscopy (TEM) specimens, the principal goal of the experimental portion is to understand the impact on void swelling which is closely tied to the defect distributions. In order to do so, the use of a pure Fe target and Fe ions are chosen to minimize secondary effects arising from chemistry changes during the course of ion irradiation.

2.1 Modelling

In order to see the differences in defect distribution, the model utilized must have a high accuracy. The Boltzmann transport equation (BTE) is utilized to calculate the point defect distributions. BTE is typically more accurate than binary Monte Carlo approaches due to the large statistical variations intrinsic to the technique. Although Monte Carlo codes may produce high accuracy the results, the computational cost is quite high. The steps of the BTE implantation are:

1) The ion range is divided into fixed intervals.
2) The electronic stopping loss is calculated when displaced atoms transition from one depth interval to the next. The amount of energy loss is determined by the actual flight distance.

3) Within a single interval, the nuclear stopping loss from nuclei-nuclei is calculated by:

$$\frac{\partial F(\mathbf{p},z)}{\partial z} = N\int\left(\frac{F(\mathbf{p}',z)d\sigma(\mathbf{p}'\to\mathbf{p})}{\left|\cos\theta_{\mathbf{p}'}\right|} - \frac{F(\mathbf{p},z)d\sigma(\mathbf{p}\to\mathbf{p}')}{\left|\cos\theta_{\mathbf{p}}\right|}\right) + Q(\mathbf{p},z) \tag{1.1}$$

where $\mathbf{p}$ is momentum vector. z is depth. $F(\mathbf{p})$ is the atom number having momentum $\mathbf{p}$. $Q(\mathbf{p},z)$ is a generation term describing recoil-created energetic target atoms having the same $\mathbf{p}$. N is the atomic density of the substrate. θ is the angle between momentum and z axis (normal to a sample surface). $d\sigma(\mathbf{p}\to\mathbf{p}')$ is the differential cross section for momentum transition of $\mathbf{p}\to\mathbf{p}'$. $d\sigma(\mathbf{p}\to\mathbf{p}')$ follows Lindhard format [41], which is given by

$$d\sigma_n(t) = \frac{1}{2}\pi a^2\left[f(t^{1/2})dt/t^{3/2}\right] \tag{1.2}$$

$$a = 0.8853a_0\left(Z_1^{2/3}+Z_2^{2/3}\right)^{-1/2} \tag{1.3}$$

$$t = TE[M_2/(4M_1)][a/(Z_1Z_2e^2)]^2 \tag{1.4}$$

where E is the initial ion energy, T is the energy transferred to target atoms, Z_1 and Z_2 are atomic numbers, M_1 and M_2 are atomic mass, for incident atoms and target atoms, respectively. $a_0(=0.0529nm)$ is Bohr radius. The function $f(t^{1/2})$ in Linhard format has various expressions, depending on the choice of interatomic potentials. The present study follows the one proposed by Wilson et al. [42], which is given by

$$f(t^{1/2}) = A\left[X^{1+C}-1-(1+C)\ln X\right](X^{2+C}-2X+X^{-C})^{-1} \tag{1.5}$$

where

$$X = Bt^{1/2}, A = 0.56258, B = 1.1776, C = 0.62680$$

It is more reasonable to calculate atom flux changes from energy values instead of transitions between different momentum values. Equation (1) is calculated for each allowed transition in the energy matrix. Nuclei-nuclei scattering favors small energy transfers, leading to a non-uniform distribution in the flux distribution. In order to better calculate the flux distribution after scattering events, the model utilizes an algorithm recently proposed to redistribute the scattered flux among neighboring energy states [43]. The resulting model provides fast and accurate defect distribution profiles.

2.2 Experimental Procedure

A high purity Fe bar (Alfa Aesar, 99.97%) was sectioned into 5 mm x 5 mm pieces with a thickness of 0.5 mm. Specimens were mechanically polished using SiC abrasive discs to a grit of 4000. Further polishing with a 0.05 um colloidal alumina solution was performed to achieve a flat and relatively damage-free surface. Irradiation was performed using 3.5 MeV Fe^{2+} ions produced by the 1.7 MV tandem accelerator at the Ion Beam Laboratory at Texas A&M University to achieve peak damage levels of 35, 70, 105 peak dpa, as calculated using the Kinchin-Pease option of the SRIM-2013 code [44]. The Fe ion beam was partially defocused and then rastered over an area of 1 cm x 1 cm to produce a uniform beam condition. The specimens were heated to a temperature of 450 °C ± 10 °C during the irradiation.

After irradiation, transmission electron microscopy (TEM) specimens were prepared using a focused ion beam (FIB) lift-out technique with a FEI Quanta 3D FEG dual beam SEM/FIB microscope. Thick lamellae were first prepared by trenching the selected region with a 30 keV Ga^+ beam. Once the lamella was thinned to approximately 1.5 μm, a micro-post was placed near the lamella and attached via Pt deposition. The lamella was then cut from the bulk of the sample, attached to a TEM grid, and thinned to 300 nm using a lower beam current. Final thinning and polishing of the lamella to a thickness of ~100 nm was performed with a 5 keV Ga^+ beam. Scanning transmission electron microscopy (STEM), high angle annular dark-field (HAADF), and

bright field images of voids were obtained on an FEI Tecnai G20 Super Twin operated at 200 kV. The thicknesses of TEM lamellae were measured using a standard electron energy loss spectroscopy (EELS) technique.

2.3 Results and Discussion

Figure 2.1 shows the predicted depth distributions of interstitials, vacancies, and Fe implants for 3.5 MeV self-ion-irradiated Fe using the BTE model. All values are normalized to a single incident Fe ion. Fig. 2.1a shows the implanted Fe distribution with a peak near a depth of 1.03 um. This is in close agreement with a SRIM calculated depth of 1.08 um. Fig. 2.1b provides a plot of the depth distribution for both vacancies and interstitials. Although the difference is quite small, the inset figures show that the distributions are, in fact, different. It is important to note that the differences become quite large when the total ion fluence is accounted for.

Fig. 2.1c plots the defect imbalance of the Fe ion irradiation by taking the difference of the vacancy density and the sum of the interstitial and injected Fe densities. Several prominent features are present in the figure. A vacancy-rich region is observed near the surface and a deeper depth near the end of ion range. An interstitial-rich region is present at a depth near the end of ion range, in line with expectations. The defect imbalance shown in Fig. 2.1c arises from the depth distribution differences between vacancies and interstitials. Since momentum transfer is favored along the incident ion direction, scattered atoms move deeper into the target and reside as interstitials, and vacancies populate shallower depths.

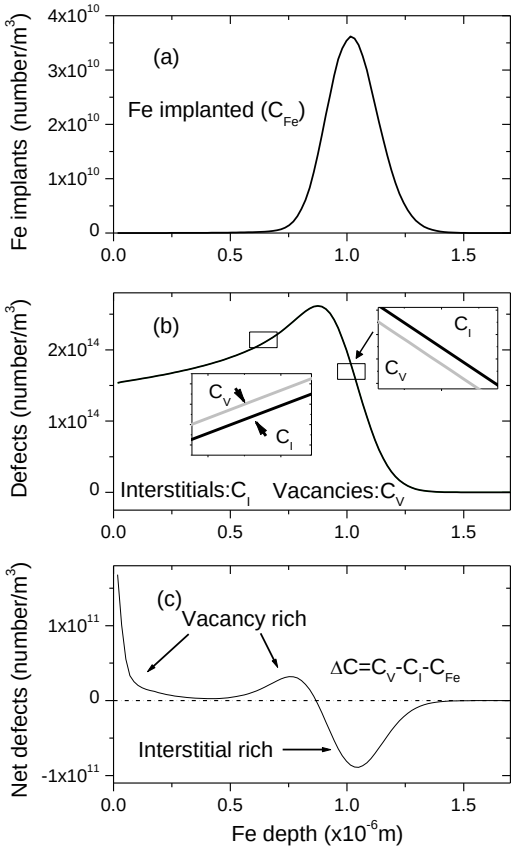

Figure 2.1 – (a) Predicted depth distribution of 3.5 MeV Fe implanted ions in pure Fe, (b) depth distributions of interstitial and vacancy concentrations, and (c) net vacancy concentration distribution (C_v-C_i-C_{Fe}). Reprinted with permission from [61] Copyright 2017 by Elsevier.

Figure 2.2 plots the distributions of vacancy-rich regions for Fe ions with energies of 0.5, 1, 2 MeV, and 3.5 MeV respectively. At all energies, the vacancy concentration gradient is large, initially decreasing from the surface and then increasing deeper into the specimen. The vacancy concentrations decrease sharply near the end of ion range. Further, the gradient increases with decreasing ion energy. This model is valid within the zero-time assumption. The imbalance effect is much more complicated to model when defect migration and annealing is introduced. Fig 2.1c shows an excess

vacancy peak at 0.8 μm near the excess interstitial peak of 1.03 μm. With long range defect migration and annealing, it is expected that the interstitials will annihilate a large portion of the vacancies, resulting in both a lower excess vacancy concentration and a distribution peaked at a shallower depth. It is further expected that in an experimental setting, the void swelling arising from vacancy agglomeration will appear at a depth between the surface and the excess vacancy peak. Since the surface is an efficient defect sink, voids are not expected to form near the surface.

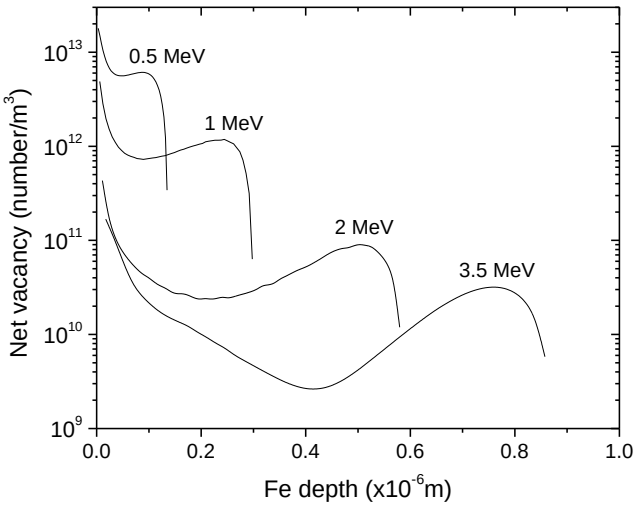

Figure 2.2 – Predicted depth distributions of net vacancy concentrations in pure iron irradiated by 0.5 MeV, 1 MeV, 2 MeV, and 3.5 MeV Fe ions, respectively. Reprinted with permission from [61] Copyright 2017 by Elsevier.

Fig. 2.3 provides TEM micrographs of the pure Fe specimens irradiated to 35, 70, and 105 peak dpa. The SRIM-calculated depth distributions for implanted Fe and dpa are superimposed in Fig. 2.3a. With increasing damage level, the average void size increased with voids appearing progressively deeper into the specimen. Even at the highest damage level, however, the void swelling was suppressed near the end of ion range.

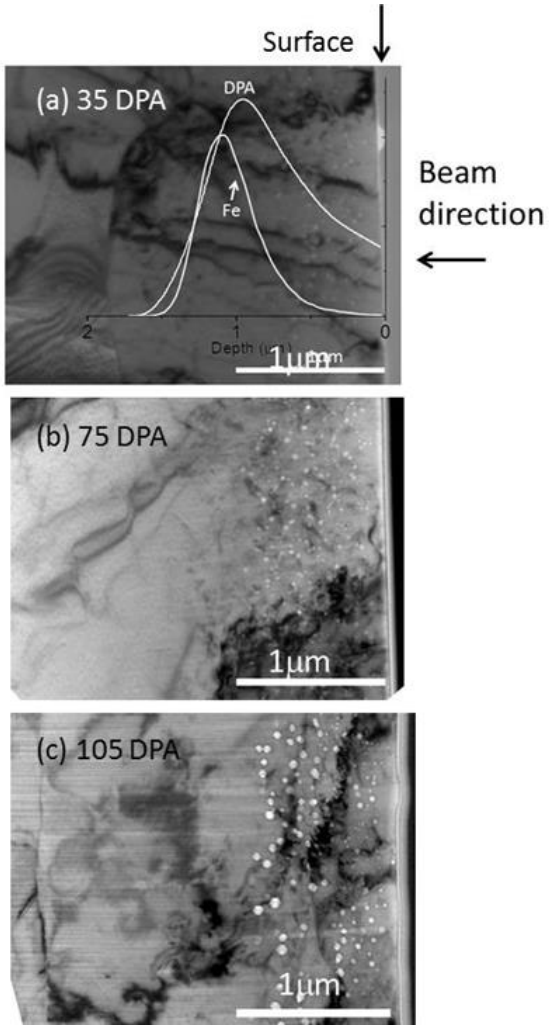

Figure 2.3 – Typical bright field TEM micrographs of pure iron irradiated with 3.5 MeV Fe ions to damage levels of (a) 35, (b) 70, and (c) 105 peak dpa. Reprinted with permission from [61] Copyright 2017 by Elsevier.

Fig. 2.4 provides the measured void swelling distribution for the Fe specimens irradiated to damage levels of 35, 70, and 105 peak dpa, respectively. At 35 peak dpa, void swelling is peaked at a value of ~0.6% at 200 nm. With increasing dose, void swelling increased monotonically accompanied by a broadening of the swelling

distribution, in good agreement with TEM observation in Fig. 3. At the highest damage level of 105 peak dpa, the void swelling distribution has two notable features. First, the development of a distribution with two peaks is observed. Although statistical variations may induce such features, numerous voids were counted (>250) to reduce error on void swelling measurements. The double peak feature, if real, requires further investigation to determine the underlying mechanism for its appearance. Second, void swelling is completely suppressed near the end of ion range. This effect has been observed in many studies [16, 45-54].

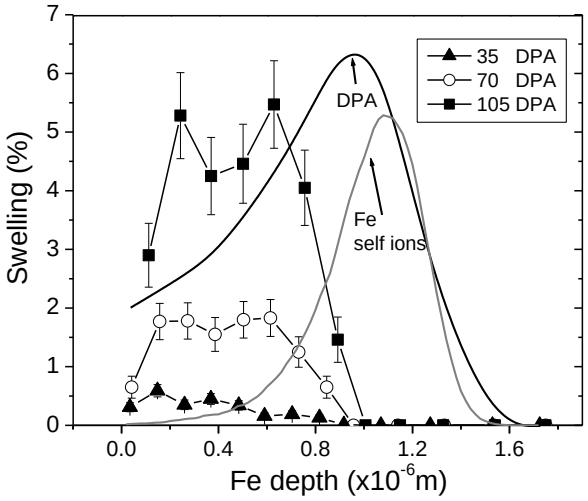

Figure 2.4 – Depth distributions of void swelling in pure Fe irradiated to damage levels of 35, 70, and 105 peak dpa, respectively. SRIM calculated range and dpa curves are superimposed on the swelling graphs for comparison. Reprinted with permission from [61] Copyright 2017 by Elsevier.

Fig. 2.5 plots the swelling as a function of the local dpa calculated by SRIM. A tangential line to the curves is drawn on the plots to calculate the swelling rate. The calculated swelling rate is ~0.26%/dpa and in good agreement with the measured swelling rate for irradiated bcc iron alloys [28].

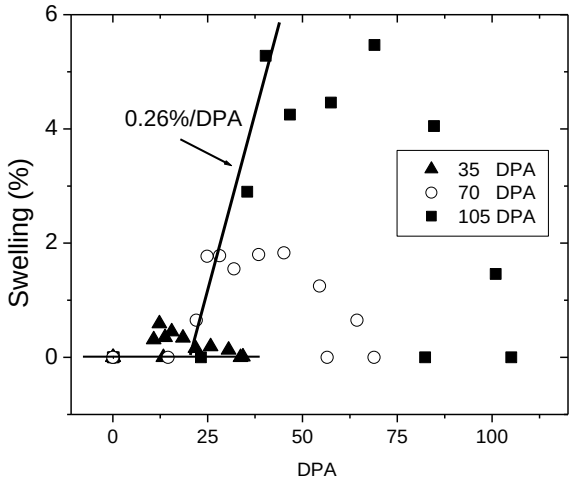

Figure 2.5 – Plot of the void swelling as a function of local dpa for pure iron irradiated to 35, 70, and 105 dpa, respectively. A line denoting the estimated swelling rate of 0.26%/dpa is shown in the figure. Reprinted with permission from [61] Copyright 2017 by Elsevier.

The present study presents some of the many possible pitfalls in accelerator-based swelling experiments. The use of FIB to produce cross-sectional TEM lamella enables a unique understanding of the sensitivity of void swelling to depth from the ion incident surface and provides a more complete picture of the microstructural evolution. Without FIB, void swelling analysis is typically performed with planar TEM lamella. Although planar TEM specimens will reveal far more voids than cross-sectional lamella, care must be taken to select the correct depth. If specimens are prepared at a very shallow depth, void swelling is reduced due to defect annihilation through the surface. On the other hand, if a region too close to the peak damage is selected, swelling will be suppressed as shown by deviation of void distributions from SRIM calculated dpa profile in the present study. This suggests that the defect imbalance may cause an

erroneous calculation of void swelling, resulting in an over- or underestimation of the swelling compared to neutron irradiation in reactors.

This study addressed the large role that differences in the depth distribution arising from ion irradiation play on the microstructural evolution. While these effects are well known in the semiconductor industry, these differences are less known in void swelling studies in metals. Using the BTE method, the depth dependent defect distribution for vacancies and interstitials were modeled. Two vacancy-rich regions, near the surface and the end of ion range, were observed and noted to deviate from the expected dpa profile. Cross-sectional TEM of ion irradiated pure Fe using 3.5 MeV self-ions confirmed this prediction. Voids appeared to develop first near the surface, followed by progressively deeper swelling at higher damage levels. In the later chapters, many of the techniques and methods used in this study will be applied not only to provide a more consistent comparison between various alloys but also to avoid many of the issues arising from the defect imbalance effect.

3. TEMPORAL DOSE RATE GRADIENTS*

The discussion and findings in the previous section showed that microstructural changes induced by ion irradiation are subject to defect imbalance effects and large gradients in defect distributions. The differences can also be framed in terms of dpa rates. For neutron irradiation, there are essentially no spatial gradients in dpa rate over dimensions comparable to grain sizes in metals, but there are two primary temporal regimes of interest. These are continuous, steady-state operation (i.e. fission reactors, Tokamak fusion reactors) and pulsed operation (i.e. inertial fusion reactors). In ion irradiation, however, spatial gradients can be very strong, often on sizes smaller than a typical grain diameter, and ion irradiation can use either a continuous, defocused beam or a focused and scanned beam, the latter often referred to as "rastering".

In order to irradiate a relatively large area compared to the ion beam diameter, beam rastering is often performed. However, ASTM E521-77 [47] strongly suggests using a defocused beam rather than a scanned beam to simulate void swelling arising from steady-state neutron irradiation. A phenomenon, often referred to as void throttling, can occur at high temperatures whereby very small void nuclei formed at a given location during the beam-on period dissolve in the longer beam-off period before the beam returns. This suggestion, however, is based on a limited set of early (1970's) experiments on pure nickel [56-58] and therefore requires additional investigation before accepting it as a universal proscription against ion beam rastering for simulation of neutron-induced void swelling behavior.

It should be noted that void nucleation is known to be very sensitive to environmental variables such as rastering, much more so than radiation-induced segregation, changes in mechanical properties, and changes in various physical properties. Thus, the ASTM E521-77 recommendation to avoid ion beam rastering is not

*Reprinted with permission from "The influence of ion beam rastering on the swelling of self-ion irradiated pure iron at 450°C", Jonathan G. Gigax, Eda Aydogan, Tianyi Chen, Di Chen, Lin Shao, Yuedong Wu, Wei-Yang Lo, Yong Yang, Frank A. Garner, Journal of Nuclear Materials 465 (2015) pp. 343-348, Copyright 2017 by Elsevier.

necessarily meant to apply to any other property changes. The current work addresses the impact of rastering at relatively low frequencies on void swelling in pure iron, which was used as a model surrogate material for more complex ferritic alloys to be studied in later irradiations. In this experiment, a limited ranged of low rastering frequencies relevant to pulsed fusion devices was used to produce void swelling and the results were compared with that produced by a steady-state, non-rastered, defocused beam.

3.1 Experiment Procedure

Specimen preparation was performed similarly to the study in the previous chapter. Samples were sectioned from a pure iron bar (99.99%, Sigma-Aldrich) to produce disks of size 4 mm x 4 mm x 0.5 mm. These disks were mechanically polished on a Dace Technologies Nano 2007 polisher using successive grits of 600, 800, and 1200 silicon carbide paper. The samples were further polished using 1 μm and 0.05 μm alumina solutions. After mechanical polishing, the samples were electropolished using a 6% perchloric and 94% acetic solution for 10 seconds to remove all residual surface damage arising from mechanical polishing. The specimens were then inspected using a scanning electron microscope to ensure an undamaged surface.

The specimens were mounted on an electrically-heated copper stage and good thermal contact was maintained using silver paste. These specimens were brought to a temperature of 450°C measured using thermocouples mounted to the stage. Independent measurements were performed to verify that the beam heating arising from either a defocused or a rastered beam was relatively low. Since most published modeling studies on pulsing and rastering focus only on isothermal conditions, care was taken to separate temporal changes in dpa rate from concurrent changes in temperature during the beam-off and beam-on periods.

The procedure used a FLIR infrared (IR) camera collecting data at 30 frames per second. Initial calibration of the sample emissivity involved matching the temperature of the stage, as measured by the thermocouple, was performed prior to commencing ion

bombardment. The temperature was then monitored by the IR camera during ion bombardment and the beam heating calculated by taking the difference of the sample temperature before and during ion bombardment. Thermally conductive samples (i.e. pure iron and graphite) exhibited a maximum temperature rise of 2-3°C for the defocused case and 4-6°C increase for the raster case. This demonstrates that the temperature rise from the two beam configurations is not substantial. Additionally, the beam uniformity was assessed using the temperature map produced by the IR camera. When compared to previous results obtained using other conventional methods, such as an optical mapping from a scintillator and a low dose Kapton implantation, the IR-derived temperature distribution shows good agreement with the uniformity established by these methods.

Iron ion irradiation was performed by using a 1.7 MV tandem accelerator with an energy of 3.5 MeV, producing peak damage levels at 1000 nm below the surface of 50 and 150 dpa, as calculated using the Kinchin-Pease option of the SRIM-2013 code [44] as recommended by Stoller and coworkers [59]. There was no gas co-injection employed in this study. The beam current was limited to 200 nA over an area of 36 mm^2, yielding a time-averaged dpa rate of 1.74×10^{-3} dpa/s, varying less than 5% over the duration of the experiment. Beam conditions are listed in Table 3.1 for all four beam conditions. The beam spot size for the defocus case was chosen to be 6 mm x 6 mm. The configuration for the defocus case involved using an electrostatic quadruple to produce a uniform beam over the desired area. To simplify the analysis, the beam involved one-dimensional rastering rather than the frequently used two-dimensional raster method.

Table 3.1 – Raster and defocused beam parameters including the duty factor, beam-on and beam-off times, and instantaneous and average dpa rates. Reprinted with permission from [66] Copyright 2017 by Elsevier.

		Beam-On (s)	Beam-Off (s)	Duty Factor	Instantaneous dpa rate when beam is on (dpa/s)	Time-averaged dpa rate through the whole irradiation (dpa/s)
Raster	15.63 Hz	0.018	0.046	28%	6.26E-3	1.74E-3
	1.95 Hz	0.142	0.370			
	0.244 Hz	1.14	2.96			
Defocus		-	-	100%	1.74E-3	

The beam size for the raster case was 2.5 mm x 4 mm and was scanned over an area of 9 mm x 4 mm, larger than the specimen size to ensure that all areas were irradiated uniformly. The ion beam was rastered using a Physicon Model RS1200 with a horizontal raster speed at 0.244, 1.93, and 15.625 Hz. The irradiated samples were characterized by cross sectional transmission electron microscopy (TEM), with specimen preparation accomplished using the focused-ion-beam (FIB) based lift-out technique. Microstructural analysis was performed using a FEI Tecnai G2 F20 instrument, operated at 200 kV.

3.2 Results

Figures 3.1(a-d) show TEM micrographs of 50 dpa (peak) specimens obtained with a rastering beam at frequencies of 15.63 Hz, 1.95 Hz, 0.244 Hz, and with a defocused beam, respectively. With decreasing rastering frequencies, void sizes tend to be smaller and densities higher. In comparison, defocusing results in larger voids. However, in all cases, voids formed with octahedral-like shapes as deduced from the observed square and hexagon shaped void projections predicted by the Wulff construction theory [60]. Figures 3.2(a-d) show TEM micrographs of 150 dpa

specimens. The observed trends in void density, sizes, and shapes at 150 dpa (peak) are consistent with observations from the 50 dpa experiments.

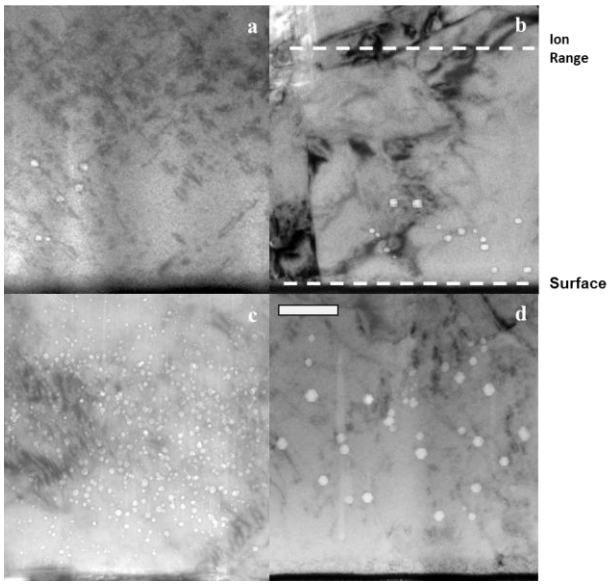

Figure 3.1 – Micrographs of void swelling for irradiation to 50 dpa at peak maximum in pure iron for rastered beams at. (a) 15.63 Hz, (b) 1.95 Hz, (c) 0.244 Hz, and a (d) defocused beam. Length of the scale bar is 250 nm. Dashed lines mark the surface and the incident ion range with the incident ion direction normal to the surface. Reprinted with permission from [66] Copyright 2017 by Elsevier.

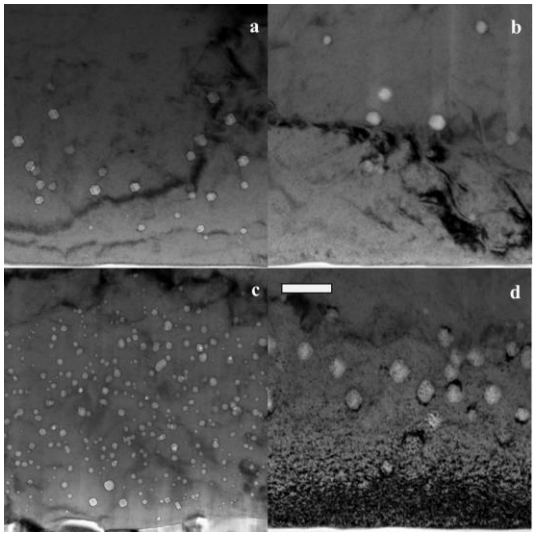

Figure 3.2 – Micrographs of void swelling for irradiation to 150 dpa at peak maximum in pure iron for rastered beams at (a) 15.63 Hz, (b) 1.95 Hz, (c) 0.244 Hz, and with a (d) defocused beam condition. Length of the scale bar is 250 nm. Reprinted with permission from [66] Copyright 2017 by Elsevier.

For a better comparison of the void swelling at 50 dpa, depth-dependent void swelling profiles were divided into two groups. Figure 3.3 compares the 15.63 Hz and 1.95 Hz rastering frequency, and Figure 3.4 compares 0.244 Hz raster and defocused beam conditions. One general trend is that with decreasing frequencies, the void distributions reach deeper into the specimen. For the lowest frequency, 0.244 Hz, the void distribution extends beyond that produced by a defocused beam. The "spikeness" of the swelling vs. depth profiles is an artifact of the relatively low number of voids and the choice of sampling statistics. Note that only a few voids were found in the 50 dpa specimen beyond ~650 nm depth in the defocus case, most likely resulting from the strong influence of the injected interstitial to suppress both void nucleation and subsequent growth [36,61]. In the rastered cases there is a progressive shortening of the voided region, moving back from 1000 to 600 to 300 nm as the rastering frequency increases from 0.244 to 1.95 to 15.63 Hz.

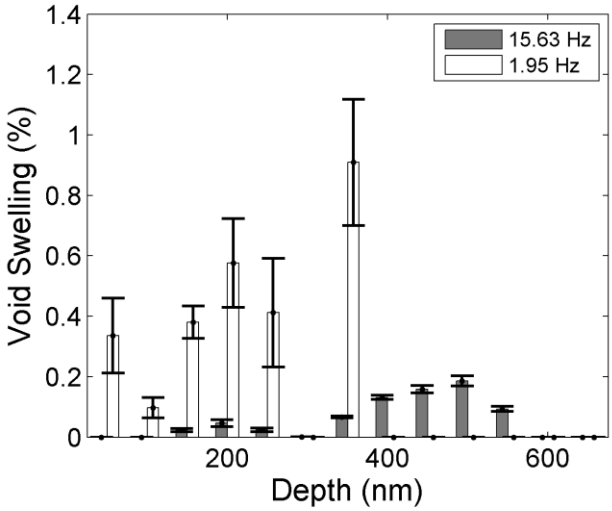

Figure 3.3 – Comparison of depth dependent swelling for 50 peak dpa irradiation with raster beam frequencies of 15.63 Hz and 1.95 Hz. Swelling data represented by each bar averaged over a 50 nm depth. Reprinted with permission from [66] Copyright 2017 by Elsevier.

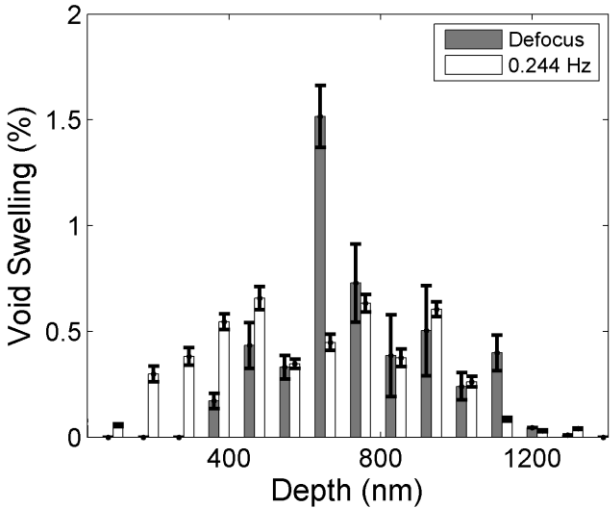

Figure 3.4 – Comparison of depth-dependent swelling for 50 peak dpa irradiation with defocused beam and raster beam frequency of 0.244 Hz. Swelling data represented by each bar averaged over a 100 nm depth. Reprinted with permission from [66] Copyright 2017 by Elsevier.

Figures 3.5 and 3.6 show the depth profiles of void swelling for the defocused and 15.63 Hz cases for 50 dpa and 150 dpa, respectively. The void depth profiles are superimposed on the normalized SRIM-calculated dpa and injected interstitial profiles. Note that at 150 dpa, voids reach deeper into the sample compared to the 50 dpa case as void nucleation at the higher dose progressively overcomes the defect imbalance effect [61]. In both cases however, void swelling is suppressed in the peak dpa region.

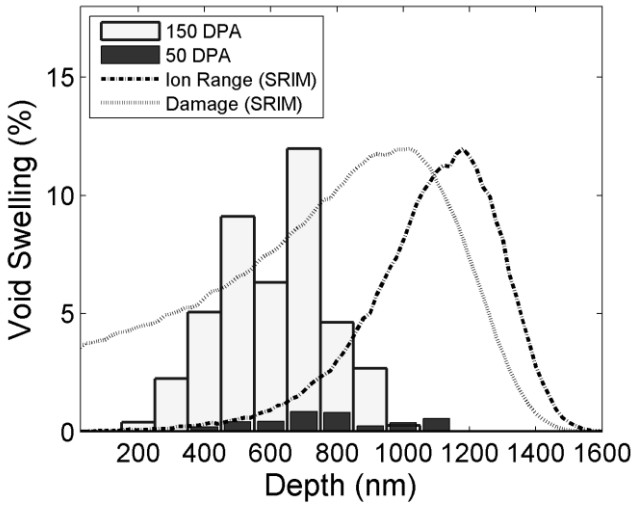

Figure 3.5 – Comparisons of depth-dependent swelling from a defocus beam for 50 and 150 peak dpa. Profiles of dpa and Fe implanted ion distributions from SRIM calculation are plotted for comparison. Reprinted with permission from [66] Copyright 2017 by Elsevier.

Also shown in Figures 3.5 and 3.6, there is a strong change in SRIM-calculated dose rate from the ion-incident surface to the peak dose position, increasing by a factor of ~3.7. In order to determine an unperturbed swelling rate between the 50 and 150 peak dpa cases without introducing differences in dpa rate, it is necessary select a depth for analysis that minimizes the influence of the specimen surface and also avoids the defect imbalance suppression zone. Therefore, swelling data was taken from the depth of 600

nm ± 100 nm, where the average dose is only ~63% of the peak value. Thus, data was actually measured at 32 and 96 dpa rather than at 50 and 150 dpa. The void characteristics and swelling are presented in Table 3.2. Although our studies are limited to two dpa values only and therefore preclude the possibility of observing non-linear swelling, the observed large differences in average swelling rate between the defocused and rastered cases are consistent. Clearly, rastering tends to suppress the void swelling rate, even when the injected interstitial effect is minimized.

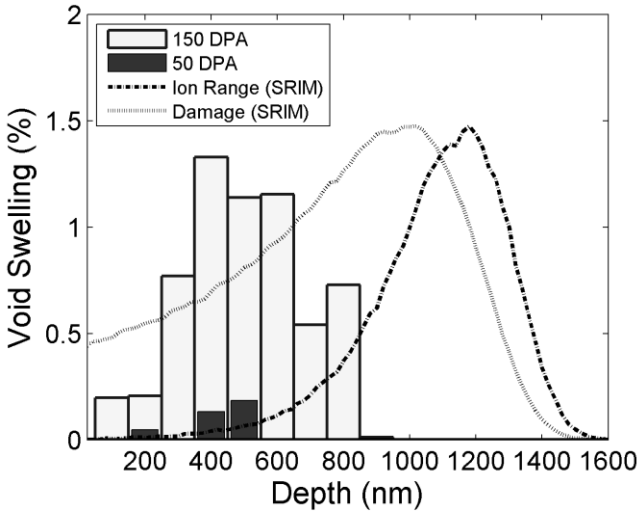

Figure 3.6 – Comparisons of depth-dependent swelling from a 15.63 Hz rastering beam for 50 and 150 peak dpa. Profiles of dpa and Fe implanted ion distributions from SRIM calculation are plotted for comparison. Reprinted with permission from [66] Copyright 2017 by Elsevier.

In Fig. 3.5, a peak swelling of ~12% at ~700 nm, along with a swelling of ~9% at a depth of 600 nm (corresponding to 96 dpa), was observed in the defocused irradiation, but the rastering-produced swelling levels are significantly lower at the same depths. As shown in Fig. 3.6, the void densities at both 50 and 150 dpa irradiations are lowest for the 15.63 Hz case, but all show a monotonic increase from 32 to 96 dpa. Overall, the depth-dependent swelling behaviors are complicated. As shown in Figure 3.7, the highest

swelling rate of ~0.12% per dpa is obtained from a defocused beam, while all rastering cases lead to significantly lower swelling values, decreasing with increasing rastering frequency. Furthermore, rastering at relatively low frequencies decreases the swelling rate quickly, with a more gradual rate of decrease occurring beyond ~1 Hz.

Table 3.2 - Void characteristics from the current study. Maximum void swelling and swelling at 600 nm ± 100 nm below the surface are provided for each set of samples. Reprinted with permission from [66] Copyright 2017 by Elsevier.

	50 peak DPA specimen				150 peak DPA specimen			
	Maximum Void Swelling (%)	Void Swelling at 600 nm (32 dpa)	Void Density (10^{14}/cm^3)	Average Radius (nm)	Maximum Void Swelling (%)	Void Swelling at 600 nm (96 dpa)	Void Density (10^{14}/cm^3)	Average Radius (nm)
15.63 Hz	0.19 ± 0.02	0.05 ± 0.01	4.79	14.2 ± 3.3	1.3 ± 0.2	1 ± 0.21	1.4	19.0 ± 6.1
1.95 Hz	0.92 ± 0.12	0	0.02	12.4 ± 4.83	5.5 ± 1.3	2.06 ± 1.25	0.746	26.9 ± 6.83
0.244 Hz	0.78 ± 0.05	0.42 ± 0.03	496	6.5 ± 3.22	5.2 ± 0.24	2.71 ± 0.18	10.9	17 ± 6.53
Defocus	1.32 ± 0.06	0.81 ± 0.08	42.5	17.4 ± 3.97	12.0 ± 0.81	8.62 ± 0.85	2.29	31.6 ± 10.2

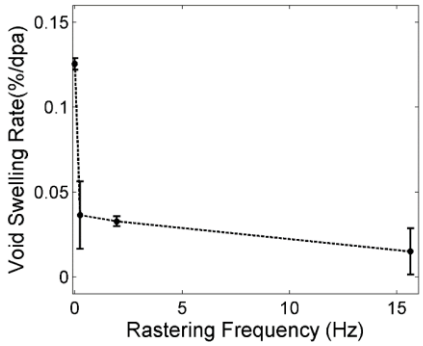

Figure 3.7 – Void swelling rates between 32 and 96 dpa as a function of rastering frequency. A frequency of zero corresponds to a defocused beam. Reprinted with permission from [66] Copyright 2017 by Elsevier.

3.3 Discussion

There are two very significant observations resulting from this study. First, in pure iron there is a strong suppression of void nucleation and growth in the region where the peak dpa and the injected interstitial overlap. At higher doses the suppression effect is overridden somewhat but is never completely overcome. This behavior was observed not only in this study but in a previous study in the current experimental series [61]. Both the present study and the previous work suggest that the swelling suppression effect requires that microstructural data be extracted from a depth removed as far as possible from the injection zone. The defect imbalance effect [61], and previously reported injected interstitial effect [36, 45-54], are known to suppress both void nucleation and void growth near the end of the ion range.

Our previous work has shown that the suppression effect arises from two contributions [61]. The first is that extra atoms are implanted into the material at the projected range, which increases the local interstitial population over that of the vacancy population. The other contribution comes from the small spatial distribution difference between vacancies and interstitials produced during the knock-on process in ion irradiation using a collimated beam. Although in damage cascade creation, the knock-on directions appear to be random, statistical analysis shows that, overall, the knock-on interactions favor momentum transfer in the forward direction, which leads to interstitial distributions slightly deeper than that of vacancies. This results in a vacancy-rich near-surface region and an interstitial-rich region near the end of range. These differences in spatial distribution lead to a dramatic suppression of void swelling near the end of ion range. As the accumulated dose increases, these influences are overcome somewhat and the void distribution pushes deeper but not completely into the full ion range. This phenomenon was also observed in a study by Kuramoto and coworkers who showed that there was a strong but not total reduction of void swelling in pure iron close to the ion deposition range, with the complication that Kuramoto used nickel ions rather than iron ions, introducing some chemical alteration in the injected region [62].

Second, it is very clear that rastering decreases the average swelling rate over the 32-96 dpa range, but there may be synergisms with other variables that were not revealed in this study. Such synergisms are suggested by the extension of the void range when going from defocused to 0.244 Hz, followed by a steady reduction in void range at higher rastering frequencies. Therefore it appears that the rastering and defect imbalance suppression effects may interact, suggesting the possibilities of more complicated dependencies at temperatures other than the 450°C employed in this study.

To provide an explanation of the underlying phenomenon involved in rastering the treatment of Ghoniem and Kulcinski [63] and Simonen [64] is used and these studies showed a significant difference between pulsed beam parameters and the resultant void swelling. The modeling was based on the defect interactions with existing void nuclei. In metals, interstitials are faster diffusing than vacancies. Further, in pure Fe with large grains, vacancy recombination with interstitials is the dominant interaction mechanism. During pulsed irradiation, interstitials are initially the primary component of the defect flux migrating towards the void nuclei, and cause their shrinkage. After a majority of the interstitials have diffused, the remaining vacancies diffuse towards and into the nuclei and thereby cause their growth. If there is a long duration between pulses, then voids begin to shrink due to vacancy emission at the void surface. Furthermore, if another pulse is introduced before significant vacancy diffusion occurs, the preexisting void nuclei will shrink further. This theory agrees with our observations that higher rastering frequencies lead to lower void swelling.

On the other hand, there is additional complexity which was not considered in the previous modeling studies. First, if stable void nuclei have already formed prior to pulsed irradiation, the effect will not be as pronounced. The previous studies assumed the existence of void nuclei prior to the irradiation. Full scale modelling is required to account for the impact of pulsing on void nucleation. Second, the existence of strong defect sinks, such as deformation-induced dislocation networks, high densities of precipitates or a high density of nanostructured grain boundaries, may alter the defect flux towards the voids, and subsequently affect the overall stability of void nuclei as a

result of competition with these other defect sinks. Third, when defect imbalance or injected interstitials are included into the picture, enhanced vacancy concentrations near the surface and enhanced interstitial concentrations near the projected range will further complicate the pulsing or rastering effect.

Within the limited accuracy associated with only two data points, our observed swelling rate of ~0.12%/dpa for the defocused beam case for pure iron may or may not be consistent with the swelling rate of ~0.2%/dpa observed in neutron irradiated Fe-Cr binary alloys [10,11]. It is probably unrealistic, however, to expect that pure iron and iron-chromium alloys must exhibit the same swelling rate. Several neutron irradiation studies have shown that chromium additions to pure iron initially cause a strong decrease of swelling [16,18,19], and one study showed that cold-worked pure iron swelled ~6% at only 3 dpa [46], a swelling rate of ~0.5%/dpa. In general, the available data shows that swelling in neutron irradiated pure iron is accelerated by cold-work and is also accelerated by irradiation at lower dpa rates [10,16,18,19,46]. For instance, Kuramoto notes that ~0.3% swelling was attained at ~1 dpa in the JMTR reactor at 450°C, but the rather large uncertainty on his quoted dose level precludes a confident statement that his swelling rate was 0.3%/dpa [62].

Finally, the applicability of our results to other irradiation conditions is constrained by two limitations. First irradiation was performed at only one temperature and the behavior might change at other temperatures. Simonen [64] notes that as the temperature is increased near the peak swelling temperature, the difference in void swelling for raster speeds becomes larger, decreasing at temperatures beyond the peak void swelling temperature. Second, it should be noted that our studies utilized relatively low rastering frequencies characteristic of pulsed fusion devices. However, many current ion irradiation facilities use rastering at frequencies ranging from 200 to 2500 Hz. If the very slow rate of decline in swelling rate beyond ~1 Hz shown in Figure 3.7 is extrapolated to such high frequencies, it appears that the swelling rate might saturate at a rather low value.

Getto *et. al.* performed a raster-no raster comparison on HT9 at 440°C to 140 dpa that support the possibility of rastering-induced void suppression at higher frequencies [65]. Ion beam rastering was performed at 1061 Hz in the vertical direction and 255 Hz in the horizontal direction, with the results compared to those produced using a defocused non-rastered beam. No voids were seen in the rastered specimen with zero or 10 appm helium preinjection, and a rather low density of small voids was seen with 100 appm helium preinjection. However, in the no raster, defocused beam condition voids were seen at larger sizes and significant densities in the specimens with 0, 10 and 100 appm helium preinjection levels, showing that, in the absence of helium, rastering completely suppresses void nucleation under these irradiation conditions.

However, previous modelling [64] suggests that increasing the raster frequency to high speeds should result in void swelling similar to that of a non-rastered, defocused beam. As noted previously, however, the applicability of this model to experimental results is not clear. At this time, however, we have no confidence that our results can be extrapolated to such higher frequencies. Additionally, at this time, our results are considered to be only applicable to pure iron and should not be extrapolated to more complex alloys. Further studies are required to explore such extrapolations.

This study clearly shows that a significant effect of rastering frequency operates on void nucleation and growth in self-ion irradiated pure iron at 450°C, with rastering leading to reduction of swelling in comparison with irradiation using a defocused, static beam. When compounded with the defect imbalance effect there is a significant suppression of swelling with the net effect varying with depth from the ion-incident surface. In order to confidently use ion bombardment as a surrogate technique to replace neutron irradiation, it appears that a defocused beam should be used. The results of this study therefore support the no-raster recommendation of ASTM E521-77 in simulating neutron damage using ion bombardment

4. COMPOSITIONAL MODIFICATION VIA COULOMB DRAG*

As discussed in previous sections, the limited range of the bombarding ions and strong internal dpa rate gradients along the ion path give rise to a variety of neutron-atypical effects [36-38,61,65]. Of these, an important neutron-atypical phenomenon involves compositional alteration along the ion path [67-69]. Furthermore, surface preparation becomes increasingly important for ion irradiation to ensure the near-surface region is reasonably free of defects and contaminants.

Shao and coworkers have recently shown that negatively-charged species in the accelerator system can be entrained into the beam by Coulomb drag effects, delivering contaminants onto the ion-irradiated area [70]. The entrainment accumulates molecules along the entire beam line, regardless of whether the target chamber is under high vacuum (e.g. $<10^{-7}$ torr) or not. Among various contaminating elements, carbon is the most crucial since carbon is known to strongly influence microstructural evolution and swelling in both austenitic and ferritic alloys [2,11]. Shao and coworkers developed and tested a filtering system for their 1.7 MV tandem accelerator comprised of three magnetic deflectors spaced ~1 m apart with liquid nitrogen cold traps located in the beam-line and target chamber [70].

The effect of beam contamination on void swelling, however, was not investigated in the previous study. In the current study HT9, an F/M alloy, was selected due to its reported low void swelling [71-73]. Ion irradiation was performed both with and without the filtering system to evaluate the impact on both composition and microstructural evolution. The present study is important to establishing a standard

---

*Reprinted from "Beam-contamination-induced compositional alteration and its neutron-atypical consequences in ion simulation of neutron-induced void swelling", Jonathan G. Gigax, Hyosim Kim, Eda Aydogan, Stuart A. Maloy, Frank A. Garner, and Lin Shao, Material Research Letters (2017) pp. 1-8, available online at http://dx.doi.org/10.1080/21663831.2017.1323808. Published by Informa UK Limited, trading as Taylor & Francis Group under Creative Commons Attribution License (http://creativecommons.org/licenses/by/4.0/).

procedure or set of best practices which impact a wide range of ion beam modification, characterization and irradiation studies.

4.1 Experimental Procedure

HT9 specimens with composition given in Table 4.1 were normalized at 1040 °C for 30 min and air cooled. They were tempered at 760 °C for 1 h, followed by air cooling. Specimens were mechanically polished to 4000 grit SiC paper and jet electropolished using a solution of 5 vol.% perchloric acid and 95 vol.% methanol at -40 °C and 20 V.

Ion irradiation was performed using 3.5 MeV Fe^{2+} ions. A defocused ion beam was utilized to produce a uniform beam with a time-averaged peak dpa rate of 1.74×10^{-3} dpa/s maintained within ±5% over the duration of the irradiation [65,74]. Specimens were fixed to the stage using a carbon-free silver paste (Ted Pella, Inc. Product #16047).

Two sets of ion irradiation were conducted. The first set of specimens were irradiated to doses up to 600 peak dpa at 450 °C and did not utilize the ion beam filtering technique. The second set utilized the filtering technique and achieved doses up to 800 peak dpa at 450 °C [70].

Transmission electron microscopy (TEM) specimens were prepared using a TESCAN Lyra focused ion beam mill [74]. Scanning transmission electron microscopy (STEM) high-angle annular dark-field (HAADF), and bright field images were obtained using an FEI Tecnai F20 Super Twin operated at 200 kV. Secondary ion mass spectroscopy (SIMS) were obtained using a Physical Electronics Model 6600 SIMS System with a 4 keV Cs beam for depth profiling of elemental carbon, oxygen, and nitrogen.

Table 4.1 – Composition of HT9 (wt.%). Reprinted from [75] under Creative Commons Attribution License Copyright 2017.

Fe	C	Cr	Mo	Si	Mn	Ni	V	W
Bal.	0.21	12.5	1.10	0.29	0.41	0.60	0.30	0.51

4.2 Chemistry modification via Coulomb drag

Figure 4.1a compares SIMS carbon profiles before irradiation, and after irradiation to 600 peak dpa with and without beam filtering. The unirradiated HT9 specimen shows a flat carbon profile with average concentration of 1.3 at.% C, in good agreement with the specified composition. Without filtering, the carbon concentration after 600 peak dpa showed enhancement throughout the entire ion range, increasing to a maximum of ~7 at.% C at a depth of 600 nm, followed by a gradual decrease with increasing depth to the nominal concentration in the unirradiated region. The carbon concentration averaged over the irradiated region was ~4 at.%.

The filtered HT9 at 600 peak dpa exhibited a maximum of ~2 at.%, significantly less than the 7 at.% in the unfiltered HT9 specimen at the same depth. The carbon profile from the filtered irradiation showed a concentration dip below the background level at 800-850 nm, a depth near the peak damage. The average carbon concentration through the ion irradiated region is approximately 1.5 at.%, in close agreement with the unirradiated specimen, indicating that the contamination is greatly minimized by filtering.

The oxygen and nitrogen profiles are provided in Figs. 4.1b and c, respectively. A thin oxide layer was observed after irradiation, but the filtered irradiation clearly showed lesser oxide growth, consistent with TEM characterization. Due to beam knock-on effects during SIMS analysis, however, the tail regions cannot be used to estimate the oxide layer thickness. The nitrogen distribution in the filtered sample shows little difference from the unirradiated sample. In contrast, the unfiltered sample has a significant nitrogen profile with its tail reaching ~1 μm depth.

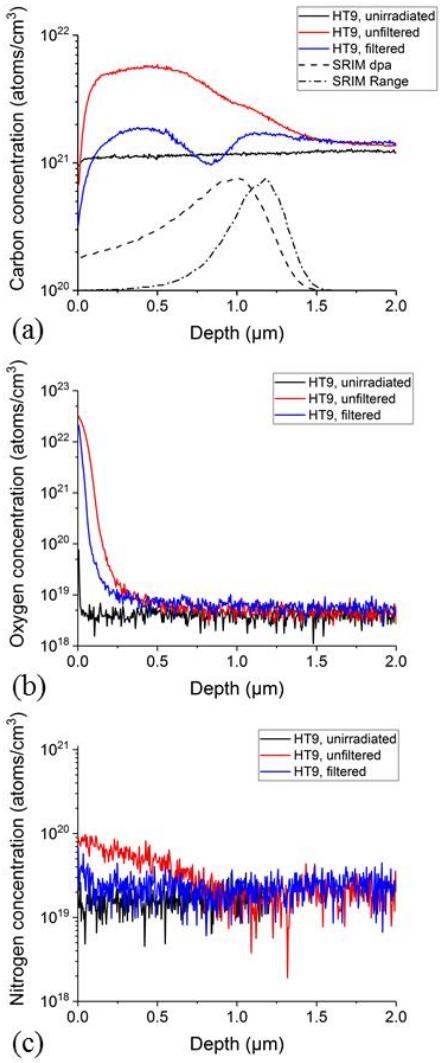

Figure 4.1 – SIMS profiles of (a) carbon, (b) oxygen, and (c) nitrogen in unirradiated and 600 peak dpa irradiated HT9, both with and without beam filtering. SRIM-calculated depth profiles of dpa and injected ions are superimposed in Fig. 1a. Reprinted from [75] under Creative Commons Attribution License Copyright 2017.

Carbon, oxygen and nitrogen possess different profiles since carbon atoms easily but strongly interact with defects, while oxygen tends to develop strong chemical

bonding with surface atoms resulting in a surface oxide layer or oxide particles. Nitrogen, however, does not interact as strongly with defects and diffuses easily. Overall, the filtering system significantly reduced or eliminated carbon, oxygen, and nitrogen contamination.

4.3 Void Swelling and Precipitation

The presence of beam-induced contaminants clearly suppresses void swelling. Figs. 4.2(a-c) compare STEM images of 200, 400, and 600 peak dpa samples without filtering. Only a few voids are observed. At doses of 200 and 400 peak dpa, the void swelling was less than 0.1% and was confined to the first 200 nm below the surface. The appearance of larger voids with ~0.5% swelling occurs at 600 peak dpa. However, voids were not observed to extend beyond this depth. A previous study has suggested that carbon atoms may alter the effective diffusivity of point defects, leading to dramatic changes in void swelling and void distribution [76]. If vacancy migration energy is slightly increased, void swelling shifts towards the surface. Both the suppressed swelling and shallow void location are believed to be related to carbon content.

Precipitates also play a key role in void swelling and, when present in high densities, can act as recombination sites and greatly suppress swelling [77-79]. Figs. 4.2(d-f) show TEM dark-field images highlighting carbide precipitates that developed in unfiltered HT9 irradiated to 200, 400, and 600 peak dpa. At 200 peak dpa, HT9 developed small spherical precipitates ~10-15 nm in diameter distributed throughout the entire ion range. At 400 peak dpa, the precipitates increased in size and evolved into needle-like structures with a high aspect ratio (1:3.5) and a diameter of ~20 nm and length of 70 nm. The density of carbides was measured to be 0.81×10^{15} cm^{-3} with a volume fraction of 0.05. A further increase in carbide density to 1.4×10^{15} cm^{-3} was observed in the 600 peak dpa specimen where the carbide precipitates were found to comprise a significant volume fraction of 0.12 in the irradiated region.

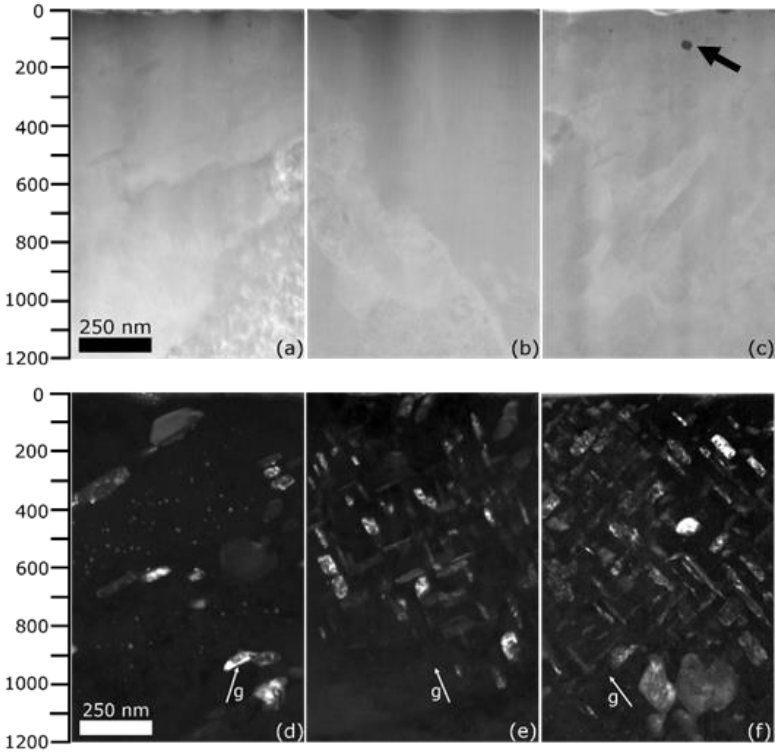

Figure 4.2 – Typical STEM-HAADF (a-c) and dark-field (d-f) images of HT9 irradiated without filtering to 200, 400, and 600 peak dpa, respectively. A depth scale to 1200 nm below the surface is provided next to (a) and (d). The g = <100> vector is labeled in the dark-field micrographs. A black arrow in (c) marks an isolated large void in the 600 peak dpa specimen. Reprinted from [75] under Creative Commons Attribution License Copyright 2017.

The majority of the precipitates observed were $M_{23}C_6$, M_7C_3, and M_3C Cr-rich carbides, and are clearly seen in Fig. 4.2f and Fig. 4.3a. Fig. 4.3b shows a typical high resolution TEM (HRTEM) image of an $M_{23}C_6$ carbide along the [112] zone axis of the particle. These carbides were observed in the unirradiated specimen along lath boundaries in the tempered martensite phase. After irradiation, a $M_{23}C_6$ carbides appeared within the grains, typically larger than other carbides observed. Plate-like M_7C_3 and needle-like M_3C carbides were observed after irradiation and comprised the remainder of precipitates formed as a result of radiation-induced precipitation

augmented by the introduction of additional carbon from the beam. HRTEM images of the M_3C precipitate along the [010] zone axis of the particle and M_7C_3 precipitate taken near the $[\bar{5}35]$ zone axis of the matrix are given in Fig. 4.3c and 4.3d, respectively. Several irradiations of HT9 and other F/M alloys at other accelerator facilities have also reported similar precipitation under irradiation and ascribed this to radiation-induced precipitation, contamination or a combination of both [80,81]. No previous study has attempted to identify and remove the source of the carbon causing the formation of the carbides.

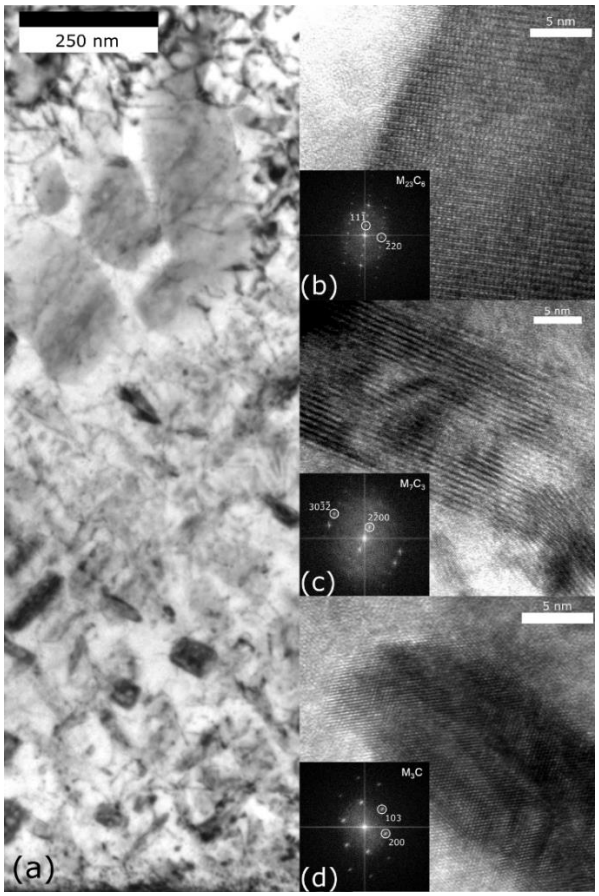

Figure 4.3 – (a) Bright-field TEM image of HT9 irradiated to 600 peak dpa without filtering, with HRTEM images of (b) $M_{23}C_6$, (c) M_3C, and (d) M_7C_3 particles. Indexed FFT images are inset in the respective figures. Reprinted from [75] under Creative Commons Attribution License Copyright 2017.

A second irradiation, employing beam filtering, was performed to reach damage levels of 200, 600, and 800 peak dpa. STEM-HAADF micrographs in Figs. 4.4(a-c) show that the filtering system induced a significant increase in swelling with dramatically different carbide precipitation behavior in Figs. 4.4(d-f). At 200 peak dpa, HT9 developed small spherical carbides of similar size and density, along with low swelling observed in the unfiltered counterpart. At 600 peak dpa, a significant increase in the population of large voids and void density were observed. Furthermore, Fig. 4.4e shows a dramatically lower carbide volume fraction of 0.014, nearly an order magnitude less than the unfiltered irradiated HT9 (Fig. 4.2f), without the development of needle-like precipitates. HT9 irradiated to 800 peak dpa exhibited further increases in void size and density with a shift in the peak swelling and a slight extension of void distribution to deeper depths. Some needle-like carbides were observed to develop within 500 nm of the surface.

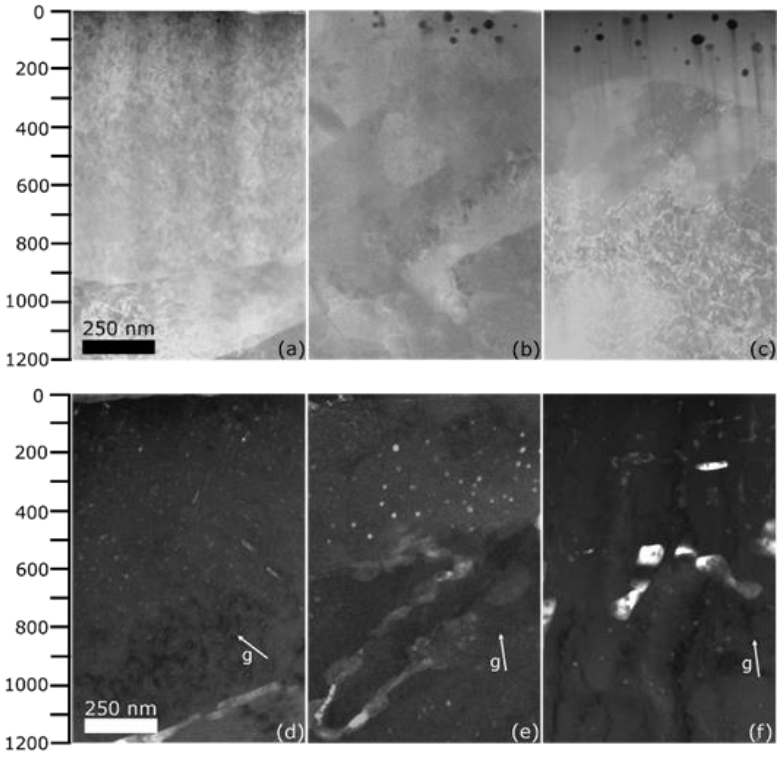

Figure 4.4 - STEM-HAADF (a-c) and dark-field (d-f) images of HT9 irradiated without a filter to 200, 400, and 800 peak dpa, respectively. The g = <100> vector is labeled in the dark-field micrographs. Reprinted from [75] under Creative Commons Attribution License Copyright 2017.

The differences in carbide precipitation and growth between unfiltered and filtered specimens are clearly seen in Figs. 4.5a and 4.5b. While both specimens showed carbides throughout the irradiated region, the volume fraction for unfiltered irradiation is greater at all depths compared to the filtered irradiation, differing by a factor of 5 for the maximum volume fraction in the specimens at 600 peak dpa. The volume fraction growth rate was calculated by averaging the carbide volume fraction plotted against the average dpa in the irradiated region. Fig. 4.5c shows that in the unfiltered specimen, the growth rate is 3.6×10^{-4} volume fraction/dpa, nearly an order of magnitude greater than the rate of 4.7×10^{-5} volume fraction/dpa observed in the filtered specimen.

Figs. 4.5d and e provide a comparison of the swelling as a function of depth for unfiltered and filtered irradiations. Void swelling in the filtered HT9 achieved a maximum swelling value ~6 times greater than the unfiltered HT9 and reached 100 nm deeper. Since voids were observed to form only within 300 nm below the surface, comparisons of the void swelling in Fig. 4.5f are plotted from the average swelling within this region, corresponding to ~35% of the peak dpa. The swelling rate in the filtered HT9 irradiation was calculated to be ~0.01%/dpa, approximately an order magnitude greater than the ~0.0011%/dpa measured in the unfiltered HT9. The filtered HT9 void swelling is in good agreement with swelling observed in HT9 after neutron irradiation in most cases [71,72]. That is, HT9 heats with 0.2 wt.% carbon exhibited similar swelling behavior to the filtered ion irradiated HT9. Despite the large variance in neutron-induced swelling, all void swelling and swelling rates are greater than the unfiltered ion irradiated HT9, with the swelling rate of the most swelling resistant HT9 heat (0.17 wt.% carbon) approximately twice that of the unfiltered HT9. Furthermore, since F/M alloys are expected to swell at 0.2% per dpa in the steady state growth stage, the observation of lower swelling rates suggests that swelling is still in the transition stage [10].

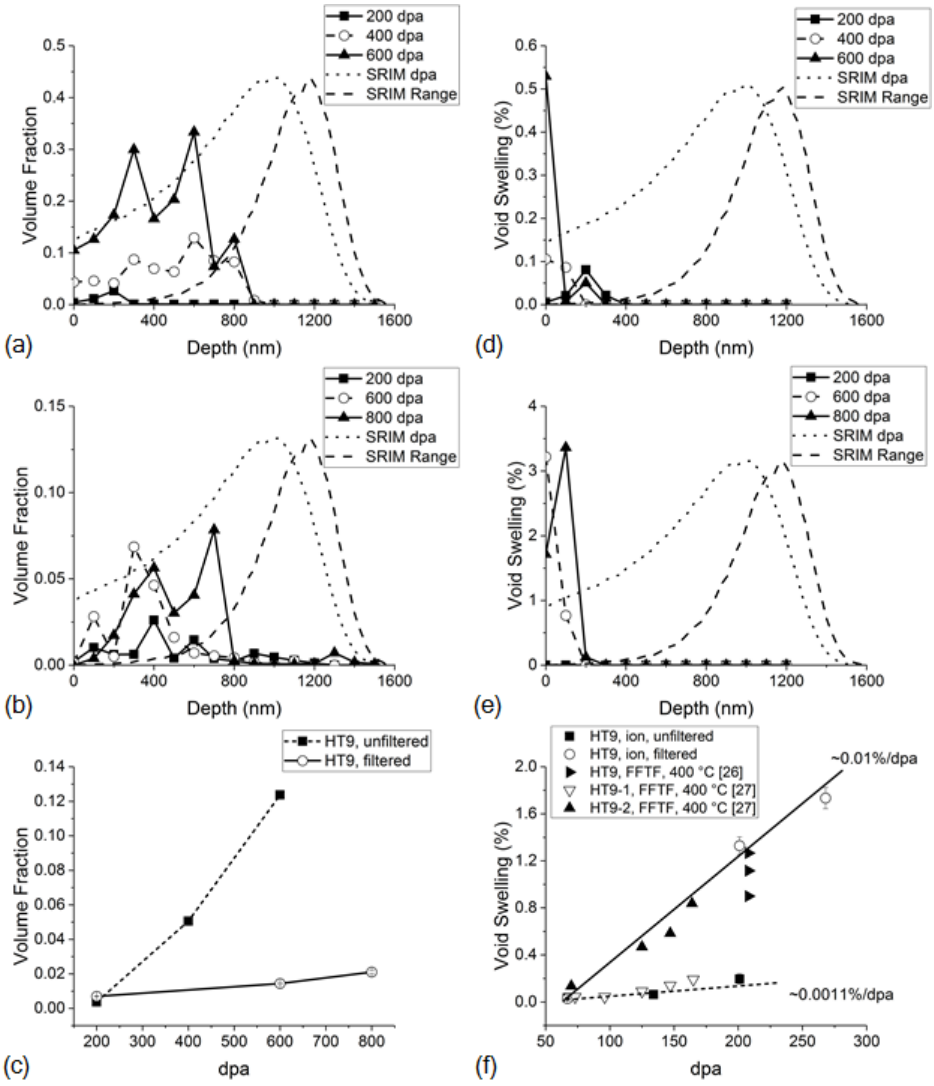

Figure 4.5 – Carbide volume fraction distributions for (a) unfiltered and (b) filtered HT9 irradiations, void swelling distributions for (d) unfiltered and (e) filtered HT9 irradiations, (c) dose-dependent carbide growth rates, and (f) dose-dependent void swelling. Neutron-induced swelling of various HT9 heats provided in (f) [71,72]. Reprinted from [75] under Creative Commons Attribution License Copyright 2017.

This study shows that contamination induced by Coulomb interaction between the beam and residual contaminants plays a dramatic role in void swelling. Without beam filtering, a high density of precipitates was observed within the irradiated region and swelling was greatly suppressed. With beam filtering to avoid/minimize

contaminants, precipitate formation was suppressed and void swelling was significantly larger. We assert that swelling suppression arises from carbon and carbides which alter the defect clustering kinetics and act as defect sinks. The present study shows the feasibility of the proposed technique as the best practice to eliminate beam contamination. When evaluating swelling data from previous studies, it will be necessary to assess the possible impact from beam contamination.

5. RADIATION RESPONSE OF T91 AT ULTRA-HIGH DAMAGE LEVELS*

The previous sections covered three neutron atypical effects that operate in a material under ion irradiation. The spatial (defect imbalance) and temporal (rastering vs. non-rastering), and large compositional modification induced by Coulomb drag (light element contamination) were found to dramatically alter the microstructural evolution. From these previous studies, a generalized procedure can be developed to minimize those effects. For the irradiations performed to ultra-high damage levels (>500 peak dpa), a static and defocused ion beam passed through the filtering system should be utilized to minimize the influence of otherwise avoidable influences. With a better understanding of these neutron atypical effects, irradiations to ultra-high damage levels can be conducted with confidence.

In the current study we focus on alloy T91, which is a ferritic/martensitic (F/M) steel that has been used extensively for non-nuclear applications in power plants, typically employed as tubing in boilers, super-heaters, or heat exchangers. There are a handful of investigations using neutron irradiation that reported on the low void swelling behavior of T91 [71,82-85]. The highest reported dose for this alloy was achieved in the FFTF fast reactor at 208 dpa and yielded a range of void swelling of 2-3% at 400°C for a set of pressurized tubes, with swelling exhibiting some variability within and between individual tubes [85]. For ion-induced swelling tests on T91, the highest reported doses were 140 and 150 dpa, yielding swelling over the range 0.04 to 0.5% in the various experiments [27 ,86]. In order to explore the suitability of T91 for advanced nuclear applications, it is necessary to explore its swelling behavior to damage levels approaching 500-600 dpa.

---

*Reprinted from "Radiation response of alloy T91 at damage levels up to 1000 peak dpa", Jonathan G. Gigax, Tianyi Chen, Hyosim Kim, Jing Wang, Lloyd M. Price, Eda Aydogan, Stuart A. Maloy, Dan K. Schreiber, Mychailo Toloczko, Frank A. Garner, and Lin Shao, Journal of Nuclear Materials 482 (2016) pp. 257-265, Copyright 2017 by Elsevier.

Since it is impractical to reach any significant fraction of this dose in a reactor, the approach used in this study is to employ self-ion irradiation and compare the results with neutron irradiated T91 and other alloys irradiated with ions under similar conditions. It is important to note, however, that for the extraction of neutron-relevant swelling data at 500-600 dpa, it is necessary to reach peak ion-induced displacement levels of ~1000 dpa due to strong suppression of swelling induced by injected interstitials in the peak dpa region.

5.1 Experimental Procedure

The heat of alloy T91 used in this study contained 9.4 wt% Cr and minor alloying elements Mo, V, Si, Ni and Nb, with compositional details given in Table 5.1. The T91 alloy was normalized at 1038°C for 0.5 h, followed by tempering at 760 °C for 0.5 h, with the specimen cooled in air after each step in the heat treatment [27]. The starting microstructure was composed primarily of a tempered martensite phase with grain sizes of ~3-5 μm and an average lath width of ~800 nm. The tempered plate was sectioned into 0.5 mm thick pieces and mechanically ground using 600, 800, and 1200 grit SiC paper. The specimens were then polished further by a 0.05 μm alumina solution followed by electropolishing with a 45% ortho-phosphoric acid, 35% sulfuric acid, and 20% de-ionized water solution for 20 s to remove the surface damage layer produced during mechanical cutting and polishing.

The irradiation conditions were performed using 3.5 MeV self-ions to damage levels of 250, 750, and 1000 peak dpa, calculated using the same procedure in the previous sections. To avoid the effects of void swelling suppression known to be caused by ion beam rastering [55,74], a defocused ion beam was utilized [65]. The ion beam was defocused and limited to 200 nA over an area of 6 mm × 6 mm, yielding a time-averaged peak dpa rate of 1.74×10^{-3} dpa/s and varying less than 5% over the duration of the experiment. F/M steels have previously been irradiated by self-ions at temperatures between 440 °C to 480 °C, a range determined to achieve the maximum swelling for the

specimen [27,78,86,87]. In the current study, the specimens were heated to 475°C during ion irradiation by mounting the samples on a copper stage with a hydrocarbon-free silver paste. The beam heating component of the temperature was measured to be ~4-5°C. The specimen temperature was kept to within ±5 °C during the irradiation. No pre-implantation or co-implantation of helium and/or hydrogen was employed. In addition to the FIB and TEM procedure given in the previous sections, additional analysis directed towards studying precipitates was also conducted.

There is a possibility that the depth dependence of swelling may be influenced by segregation-induced compositional changes arising from interaction of solutes with the displacement gradients along the ion range. Therefore, two atom probe tomography (APT) specimens were prepared from the T91 specimen irradiated to 750 peak dpa via a standard lift-out procedure [88] with an FEI Quanta 3D FEG Focus Ion Beam (FIB). The specimen at this dose level was chosen to avoid a heavily voided microstructure while still capturing the impact of an ultra-high damage level. APT specimen fabrication was controlled to a specific region that was within a depth region of 400-600 nm below the ion incident surface, consistent with the depth of greatest interest in this study since the maximum amount of swelling will be shown to occur at this depth at the highest peak damage level of 1000 dpa.

A final cleaning step using 2 kV Ga^{+} beam was carried out to reduce the FIB ion beam damage during specimen fabrication. APT measurements were performed using a local electrode atom probe (LEAP 4000 XHR) at the Environmental and Molecular Sciences Laboratory at Pacific Northwest National Laboratory. All data were collected under vacuum of 1×10^{-11} Torr at 40 K with a detection rate of 0.5 %, laser energy of 70 pJ/pulse, and laser pulse frequency of 200 kHz. The Interactive Visualization and Analysis Software (IVAS) from CAMECA was used for data reconstruction and analysis.

Table 5.1 - Composition of T91 used in this study. Reprinted with permission from [74] Copyright 2017 by Elsevier.

	Fe	Cr	Mo	V	Mn	C	Si	Cu	Ni	Al	Nb	N	P	S
wt%	Balance	9.38	0.91	0.19	0.38	0.085	0.34	0.08	0.097	0.032	0.08	0.042	0.019	0.0008

5.2 Void Swelling Analysis

Fig. 5.1 (a-c) shows typical STEM-HAADF micrographs after irradiation to 250, 750, and 1000 peak dpa, respectively. Voids were clearly observed in all specimens, but their sizes and distributions varied significantly. At the lowest dose (250 peak dpa), small voids were mainly located in the near surface region at a depth between 100-300 nm where the local dose ranged from 80 to 100 dpa. At 750 peak dpa, the voids were larger and the void distribution was observed deeper into the specimen at 900-1000 nm where the dose ranged from 725 to 750 dpa. For the highest dose of 1000 peak dpa, larger voids up to ~110 nm in diameter were observed and the void distribution again reached to 900-1000 nm ranging from 950 to 1000 dpa. The average lath width of ~800 nm and grain size of ~3-5 um observed in the unirradiated T91 was not changed significantly in the T91 specimens irradiated to 250 peak dpa. At 750 and 1000 peak dpa, however, the lath width was observed to increase to ~1 um, coincident with a large increase in void swelling. A summary of the void statistics averaged over the 400-600 nm range is provided in Table 5.2.

Table 5.2 - Void characteristics from the current study. Maximum void swelling and local swelling at the interval of 500 nm ± 100 nm below the surface are provided for each set of samples. The dpa level, void radius and void concentration are averaged within the interval. Reprinted with permission from [74] Copyright 2017 by Elsevier.

Peak dpa	Maximum void swelling (%)	Void swelling at 400-600 nm (%)	Average void radius (nm)	Average void concentration (10^{14}/cm^3)
250	1.00 ± 0.06	0.04 ± 0.01	12.0 ± 4.79	0.68 ± 0.04
750	6.20 ± 2.15	2.77 ± 0.96	17.3 ± 6.97	2.55 ± 0.27
1000	22.5 ± 2.22	17.3 ± 1.86	37.8 ± 6.99	4.58 ± 0.05

The expansion of the void distribution from the front near-surface region to a deeper depth with increasing dose has been observed previously [61,65,89] and can be explained by the concept of defect imbalance [61]. This phenomenon combines the effects of forward scattering of the incoming ion and that of the injected interstitial effect, both of which are neutron-atypical phenomena arising in self-ion irradiation. Due to forward scattering of interstitials and the extra atoms introduced by ion irradiation, spatial differences arise in the local vacancy and interstitial distributions. The near-surface region is slightly vacancy-rich, while an interstitial-rich region is created near the peak damage region. Thus, void formation is promoted early at shallow depth, while being strongly suppressed in the peak damage region. The highest swelling region eventually lies in-between these two regions, shifting deeper from the surface with increasing damage, but eventually stopping at approximately half of the range of implanted Fe ions. In general, this near-surface swelling behavior has been observed not only in our various studies, but also in those of other researchers [27,86].

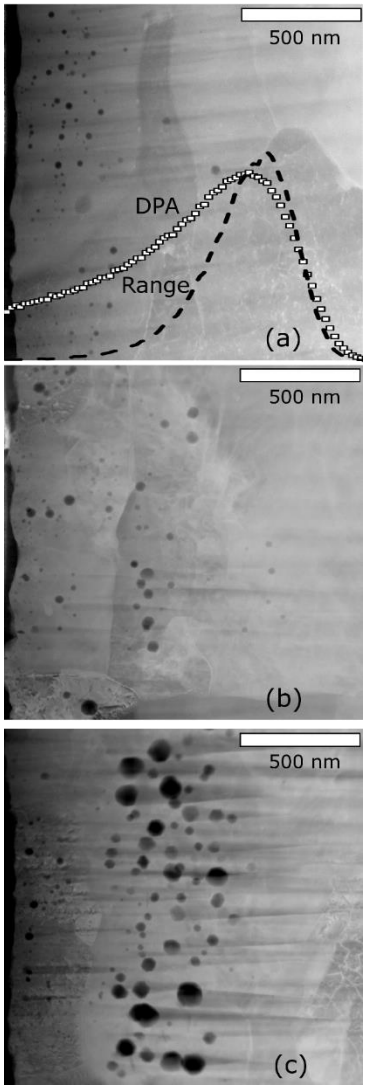

Figure 5.1 - Typical STEM-HAADF micrographs of selected areas of T91 ion-irradiated to a peak dose of (a) 250, (b) 750, and (c) 1000 dpa. An overlay of the SRIM-calculated ion range and damage distribution curves is provided in (a). Reprinted with permission from [74] Copyright 2017 by Elsevier.

Fig. 5.2 compares the measured void swelling as a function of depth for all three damage levels. The SRIM-predicted Fe ion range and dpa profiles are also plotted for comparison. Initially, swelling occurred only within 300 nm of the surface, reaching a maximum of ~1% for the 250 peak dpa specimen. At 750 peak dpa, the void swelling

reached a maximum of ~6.2% at an approximate depth of 700 nm and 740 local dpa. At 1000 peak dpa, the maximum swelling was ~22% at 550 dpa located between a depth of 450 nm and 550 nm (475 to 625 local dpa), with large voids extending from a depth of 300 nm to 900 nm (420 to 950 local dpa).

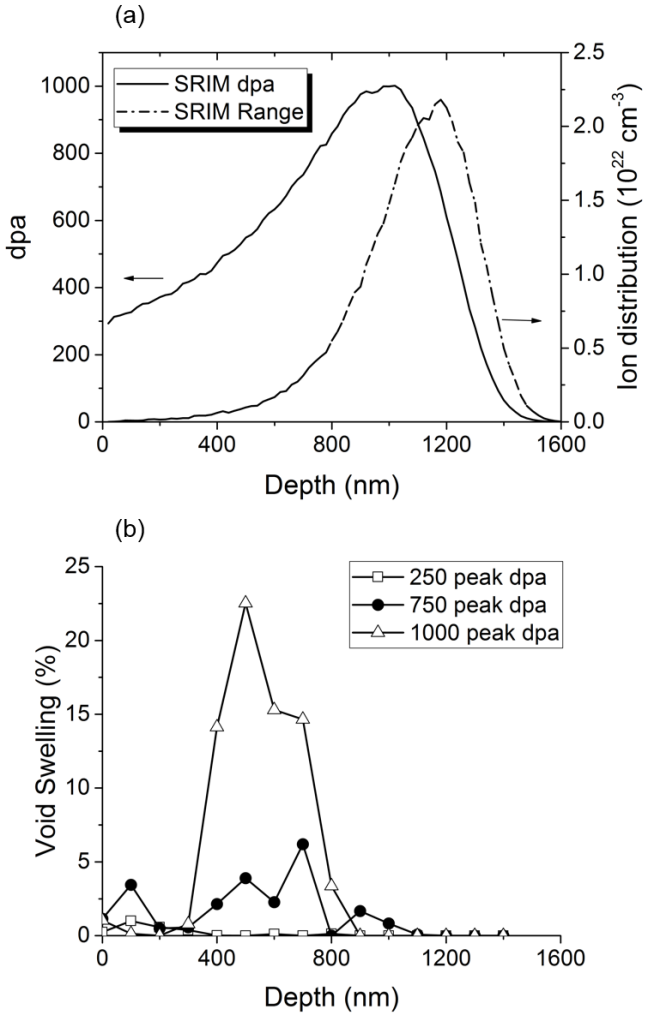

Figure 5.2 – (a) Profiles of dpa and Fe implanted ion distributions from SRIM calculations plotted for a dose of 1000 peak dpa. Arrows next to curves indicate the respective axes. (b) Void swelling as a function of depth for T91 specimens irradiated to peak dose of 250, 750, and 1000 dpa. Local swelling levels were calculated for 100 nm intervals of depth. Reprinted with permission from [74] Copyright 2017 by Elsevier.

Depth-dependent swelling analysis provides additional insight into other possible mechanisms that can influence void swelling. Although the aforementioned defect imbalance effect plays a large role in the observed swelling behavior of ion irradiated materials, there is another neutron-atypical effect that arises from the relatively large variation in the dpa rate over the ion range. Note in Fig. 5.2 that there is a factor of ~4 increase in dpa rate from the ion-incident surface to the peak damage rate position. Garner and Guthrie [38] suggested that such a difference in dpa rate with depth constituted an "internal temperature shift" that could produce a variation in the duration of the transient regime and/or swelling rate as a function of depth from the surface. It is known that the transient regime of neutron-induced void swelling in austenitic alloys is strongly dependent on dpa rate, increasing in magnitude with increasing dpa rate [1,2]. There is, however, only limited evidence that a similar dependence may occur in neutron-irradiated ferritic iron-base alloys [90]. Earlier studies using several ion-induced damage rates have shown that a similar shift in the transient regime occurs during ion bombardment of austenitic alloys [91-93].

The most dramatic feature of the swelling behavior with depth is the total absence of voids in the region of highest dpa levels. As the dose increases, it can be seen that the injected interstitial effect was gradually overcome, with swelling observed deeper in the foil. However, as the injected population increased more rapidly, voids could not nucleate beyond ~900 nm. Although this absence can be ascribed to the defect imbalance and dpa rate effects mentioned previously, this absence is primarily a consequence of the former on void nucleation, where the incident ion serves as one-half of a Frenkel pair without an accompanying vacancy [36,47-54]. While this slight imbalance might seem to be very small, it has been demonstrated theoretically to have a very strong impact on suppression of void nucleation [47].

Fig. 5.3 provides void swelling values taken from selected depth intervals as a function of the average local damage level in that interval. Swelling was measured from

sub-regions of 200-400, 300-500, 400-600, 500-700, and 600-800 nm, each with a 200 nm thickness (compared to 100 nm in Fig. 2) and dose rates of $0.72x10^{-3}$, $0.83x10^{-3}$, $0.96x10^{-3}$, $1.11x10^{-3}$, and $1.29x10^{-3}$ dpa/s, respectively. First, it is clear that swelling at each depth range showed a transient incubation dose with low-rate swelling, followed thereafter by an acceleration in swelling. Second, void swelling, at all dose rates, exhibited an increasing incubation period at deeper depths due to combined effects from both higher local dpa rates and the growing injected interstitial effect. Similar dpa rate or flux effects have been observed previously in ion irradiation [94,95] and neutron irradiation studies [2,71,96,97].

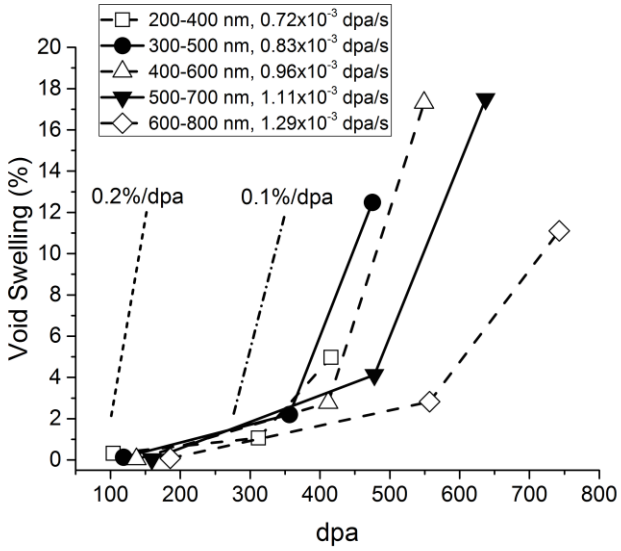

Figure 5.3 - Void swelling as a function of local damage level averaged over selected depth intervals of 200 nm thickness with swelling rates of 0.1 and 0.2%/dpa included on the figure for comparison. The transient period of swelling appears to increase with increasing dpa rate. Reprinted with permission from [74] Copyright 2017 by Elsevier.

While it is problematic to establish a post-transient swelling rate from only three data points spanning both the transient and post-transient regimes, the highest measured ion-induced swelling rate between the last two high-dose data points is ~0.11%/dpa,

which is less than the ~0.2%/dpa rate observed for body-centered cubic (bcc) iron-base metals following neutron irradiation. Hence, even at the highest damage level of 1000 peak dpa in this study, the swelling cannot be stated to have fully evolved into the steady-state void swelling stage. However, as shown in Fig. 5.4, the shift in transient duration with depth in T91 shown in Fig. 5.3 was also observed by Aydogan *et al*. in a ferritic alloy EK-181 along the ion path as the dpa rate increases [89]. In this case, the post-transient swelling rate was clearly observed to be ~0.2%/dpa. Additionally, it should be noted that Aydogan's data in Fig. 5.4 also show a pronounced extension of the transient regime with increasing depth, arising from the combined influence of increasing dpa rate and increasing influence of the injected interstitial. Our observation of an extension in transient duration with increasing depth and therefore increasing dpa rate was also provided by Whitley and coworkers who irradiated pure nickel with 14 MeV Ni ions [93], providing additional confirmation of the "internal temperature shift" concept.

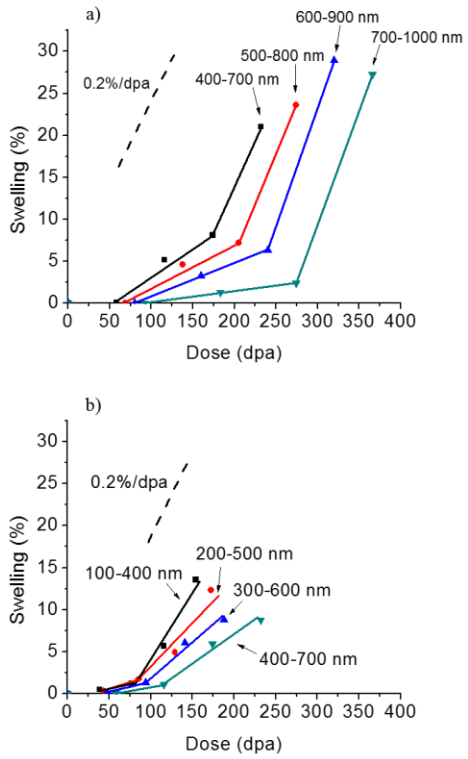

Figure – 5.4 Swelling of (a) annealed and (b) severely deformed EK-181 as a function of dpa but extracted from different depth regions. These irradiations were performed under conditions identical to that used for T91 in the current study. The tendency to approach a swelling rate of ~0.2%/dpa and also to exhibit longer transient duration before changing to the 0.2%/dpa rate with increasing depth are clearly shown. Data were provided by E. Aydogan in advance of publication [89]. Reprinted with permission from [74] Copyright 2017 by Elsevier.

Other non-rastered ion studies conducted on pure iron [65] and several ferritic-martensitic alloys [87] were observed to develop a post-transient swelling rate of ~0.2%/dpa, in agreement with the neutron-induced swelling rate. Two of these observations are shown in Fig 5.7. These observations of 0.2%/dpa were made on two different accelerators, operating at two different conditions of dpa rate and ion energy, one located in the Ukraine and the other in Texas, signaling the possible reproducibility of this swelling rate in both ion and neutron irradiations.

In a series of recent ion irradiations using rastered beams at the University of Michigan the swelling rates appear to be much lower, proceeding at rates of ~0.03%/dpa or less, possibly reflecting the raster-suppression effect on swelling [65,99]. Indeed, one study in this series involving a direct comparison between raster and no-raster irradiation showed very clearly the strong effect of rastering to suppress swelling at the scanning rates used in that study [65]. A similar study conducted on pure iron at much lower scanning rates also showed raster-suppression of swelling [66]. It is premature at this time, however, to directly ascribe the lower swelling rates only to rastering. Further investigation is required to confirm this possible linkage.

As shown in Fig. 5.2 the highest local swelling for T91 in this experiment is ~22% at 500 nm depth with a local damage level of ~550 dpa, suggesting that T91 is a rather swelling-resistant alloy compared to other ferritic or ferritic-martensitic steels. For later comparisons with neutron-irradiated T91 and other ion-irradiated alloys, the depth region from 400-600 nm was chosen to extract swelling data. This depth region exhibited the most swelling, suggesting that it has the least influence from the surface effect and the injected interstitial suppression of void nucleation.

Fig. 5.5 plots void sizes and void concentration changes as a function of local dpa values. The void statistics are obtained by averaging over the depth region of 400 to 600 nm. Both void sizes and void concentration increase with increasing damage levels, without any indication of saturation. At the highest dose, average void diameters span from ~5 nm in the shallow depth region (<400 nm) to an average of ~35 nm at deeper depths (400 to 600 nm). While some large voids were observed within this region, on the order of 100 nm, several smaller voids (~10-20 nm) were also present.

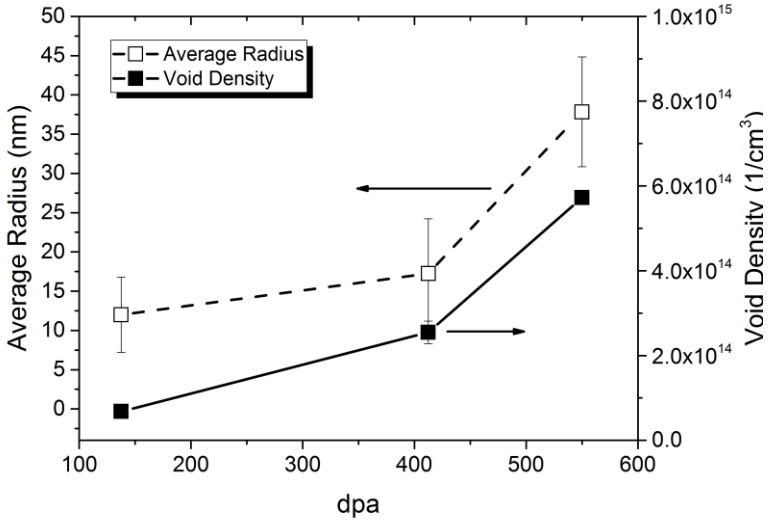

Figure 5.5 - Plot of the average void radius and concentration as a function of local dpa for the depth region of 400 nm to 600 nm. Arrows are shown to indicate corresponding axis. Reprinted with permission from [74] Copyright 2017 by Elsevier.

Fig. 5.6 compares the swelling in the region of 400-600 nm with that observed in various neutron irradiation experiments [71,82-85]. Note that all ion-induced swelling points in Fig. 5.6 are plotted as a function of local dpa. For 250, 750 and 1000 peak dpa irradiation, the corresponding average dpa values in the void swelling analysis region are 140, 410, and 550 dpa, respectively. The comparison between neutron and ion data in Fig. 6 must recognize that there are variations in composition and fabrication of the various T91 heats for both ion and neutron irradiations. Furthermore, a range of dpa rates from 10^{-8} – 10^{-6} dpa/s were reported for the neutron irradiated specimens depending on the sample position in the reactor core [95,96]. Ignoring differences in composition, however, ion irradiation at high dpa rates ($1.7x10^{-3}$ dpa/s) appears to delay the onset of swelling compared to that under neutron irradiation, again suggesting the likelihood of the dependence of transient duration on dpa rate. As mentioned previously, various studies have shown that increases of dpa rate under both neutron and ion irradiation lead to an extension of the void swelling regime for austenitic alloys [1,2,91,95,96,100,101].

There is one indication that a similar effect occurs in the Russian F/M alloy EP-450 [90], but there is insufficient data at present to ascribe the longer ion-induced transient of T91 (as shown in Fig. 5.6) solely to the differences in dpa rate.

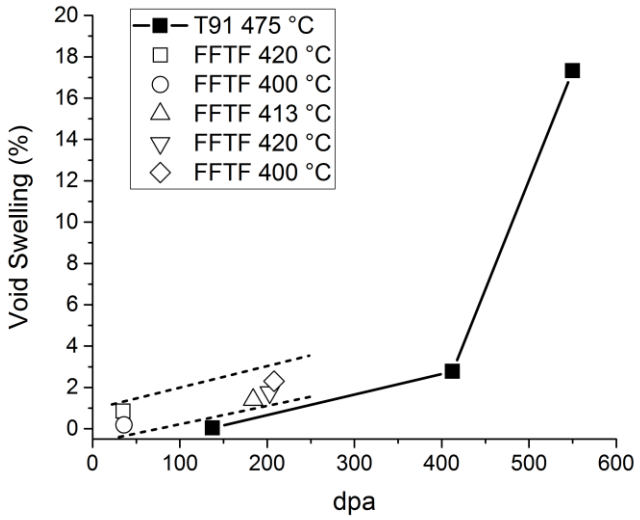

Figure 5.6 – A comparison between the swelling behavior of various heats of T91 irradiated in FFTF [71,82-85] and that of ion-irradiated T91 at a depth of 400-600 nm (present study). Reprinted with permission from [74] Copyright 2017 by Elsevier.

Fig. 5.7 compares our results on T91 with various ion irradiated alloys, including one austenitic alloy (18Cr10NiTi) and two F/M alloys (duplex EP-450 and cold-worked HT-9). These three alloys were irradiated at Kharkov Institute of Physics and Technology in the Ukraine by 1.8 MeV Cr^{+} ions with a local dose rate of $1x10^{-2}$ dpa/s at comparable temperatures and also without helium implantation. The 18Cr10NiTi alloy exhibited a steady-state swelling rate of ~1%/dpa after a very short incubation period, in good agreement with neutron data [11,102,103].

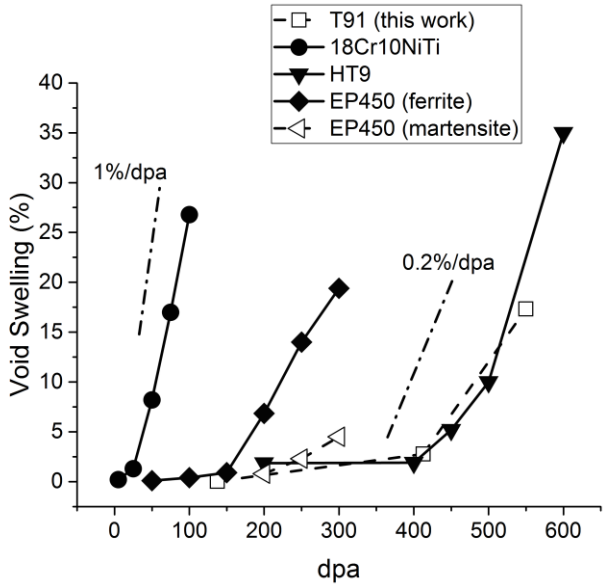

Figure 5.7 - Comparison of the void swelling in T91 with that of other ion-irradiated alloys. Reprinted with permission from [74] Copyright 2017 by Elsevier.

Fig. 5.7 also shows that cold-worked HT-9 exhibited an incubation period of ~400 dpa before accelerating to a swelling rate on the order of ~0.2%/dpa, in agreement with behavior expected for F/M alloys [10,87]. This ion-induced swelling rate was also observed in ion-irradiated ferrite grains of duplex alloy EP-450 in the range 150-300 dpa, although the swelling rate of tempered martensite grains was somewhat lower but still increasing at 300 dpa. The swelling rate of T91 appears to be increasing at higher dose, but in this experiment had not yet convincingly approached the anticipated 0.2%/dpa swelling rate, reaching only a maximum of ~0.11%/dpa.

5.3 Microchemical Evolution

As addressed earlier, neutron-induced void swelling is sensitive to the overall starting composition and the details of distribution of individual elements. It is also known that radiation causes redistribution of the various elements in both bcc and fcc

iron-base alloys and often the redistribution precedes and accompanies the onset of void swelling [1,2]. Additionally, radiation-induced segregation and possible subsequent precipitation caused by ion-induced gradients in dpa levels with depth may modify the local composition vs. depth profiles, as theoretically modeled in several recent papers [104,105]. It should be noted that there is also a significant time-dependent alteration of the composition at the end of range due to the implanted Fe ions, an effect that becomes more pronounced at the high doses explored in this experiment, reaching double-digit concentration levels at 1000 dpa.

Table 5.3 provides composition data obtained by APT analysis on T91 irradiated to 750 peak dpa taken at depths between 400-600 nm, corresponding to an average local dpa of 410 dpa. For most solutes, there was notable depletion from the matrix compared with the nominal level expected for unirradiated T91, especially for Cr, Mn, and Si. Modelling studies indicate that Cr especially will be redistributed along the ion path [104,105]. Such a large reduction in Cr in the 400-600 nm region is currently thought to be primarily a consequence of the surface and dpa rate gradients, with a lesser influence of precipitation since no significant amount of radiation-altered precipitation was observed. This supposition requires further investigation, however.

Table 5.3 - Composition of T91 obtained by APT at a depth from 400-600 nm. The measured composition for unirradiated T91 for selected solutes is provided for comparison. Reprinted with permission from [74] Copyright 2017 by Elsevier.

wt%	Cr	Mo	Mn	V	Nb	Ni	Si	Cu	C	S
Tip #1	2.62	1.41	0.05	0.23	0.00	0.10	0.01	0.05	0.00	0.005
Tip #2	2.80	0.68	0.10	0.16	0.00	0.34	0.01	0.11	0.00	0.01
Nominal	9.38	0.91	0.38	0.19	0.08	0.097	0.34	0.08	0.085	0.0008

On average, both Cu, Mo, and Ni exhibited slight enrichment in this region along with an elevated presence of S. The mechanism for the observed depletion and enrichment of the various solutes is thought to be due to a combination of inverse-

Kirkendall and solute-drag effects produced by both the influence of the surface and the dpa rate gradients [104-107]. It can be reasoned from the earlier compositional studies on void swelling that this modification may result in slightly different void swelling behavior than that of the base alloy [17-20]. It is expected, then, that the void swelling at different depths will also respond differently to the evolving depth-dependent differences in composition as the ion irradiation proceeds. In this paper we present the first results that suggest that microchemical segregation arising from both dpa gradients and precipitation may play a role in the observed swelling vs. depth profiles.

From Fig. 5.8, it can be readily seen that there are a few precipitates enriched in Si, Ni, Mn, and Cu within the analysis volume. Differences in solute concentrations suggested that there are two kinds of precipitates. The precipitates labeled A are primarily composed of Ni, Si, and Mn with a slight enrichment of S. It is possible that some of these precipitates may have formed during metallurgical production from the addition of Mn to remove S from the matrix during fabrication. However, these precipitates have also been observed to form in T91 at low proton and self-ion doses [108], suggesting these to be primarily the result of irradiation. Precipitates labeled B are rich in Si, Ni, Mn, and Cu, enrichments similar to an intermetallic phase known as the G-phase that can form in both irradiated ferritic and austenitic alloys.

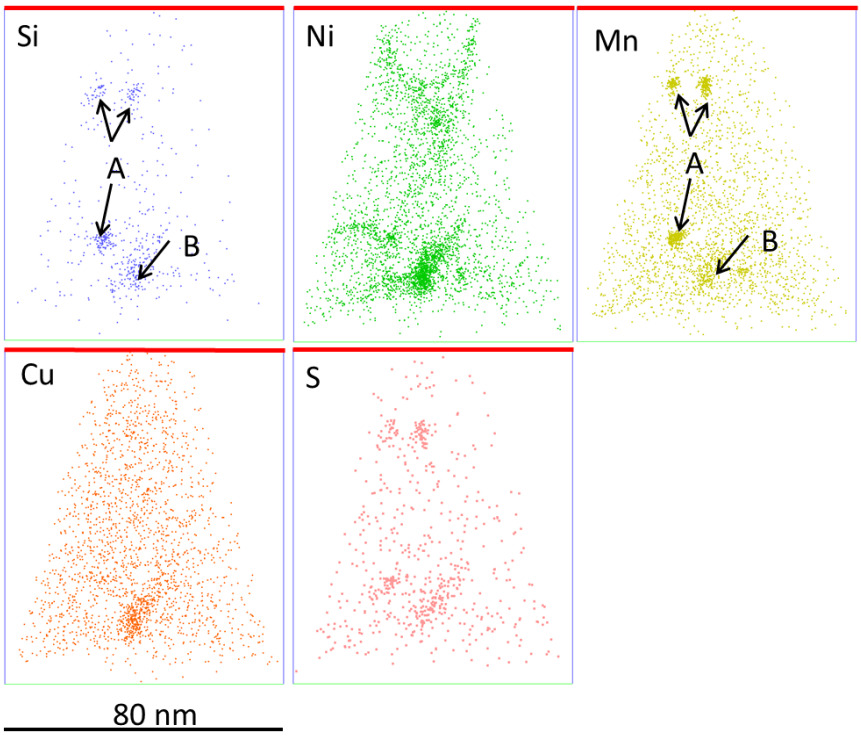

Figure 5.8 – Solute distribution obtained by APT from the first tip prepared from the T91 specimen irradiated to 750 peak dpa, showing two types of precipitates. Note that the red border at the top indicates the ion-incident surface. The tip length shown above is approximately 95 nm. Reprinted with permission from [74] Copyright 2017 by Elsevier.

Fig. 5.9 provides solute mapping similar to Fig. 5.7 on a second APT tip, but extends the analysis to both Cr and P. There are two readily observed precipitate sizes seen in the reconstructed data. The smaller precipitates were found to be similar in composition to those precipitates labeled A in Fig.8. The larger precipitate was Cu-rich with an enrichment of Si, Ni, Mn, and Cr. This precipitate featured a complex structure and showed Cu enrichment near its periphery with a Si and P-rich core. Precipitates of this size and structure were notably absent in the first tip.

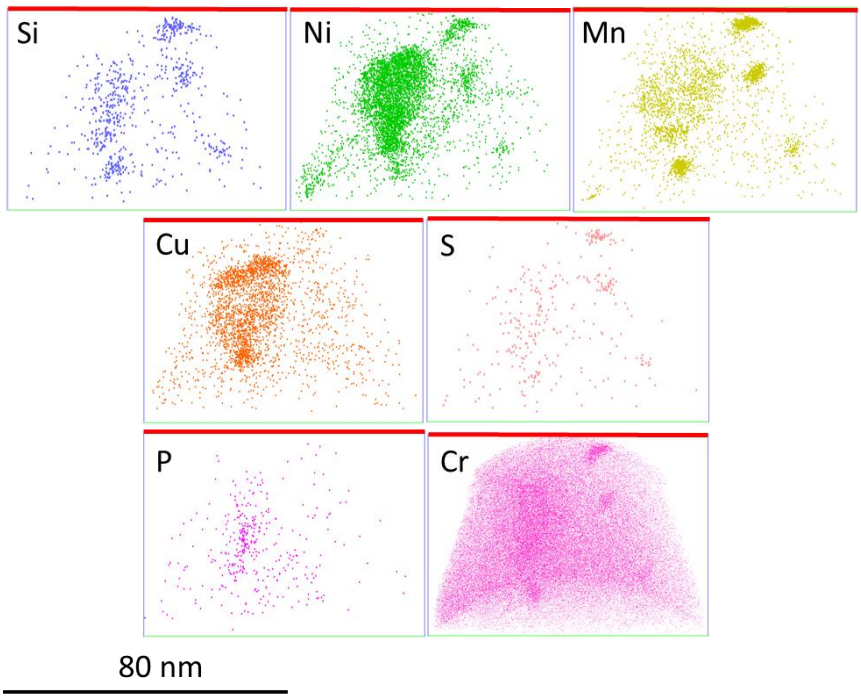

Figure 5.9 - Solute distribution obtained by APT from the second tip prepared from the T91 specimen irradiated to 750 peak dpa, showing two types of precipitates. Note that the red border indicates the ion-incident surface. The tip length is approximately 40 nm. Reprinted with permission from [74] Copyright 2017 by Elsevier.

Both Figs. 5.8 and 5.9 clearly show radiation-induced precipitation occurring in T91 at a high damage level. While precipitation was observed in neutron-irradiated T91 [84], the gradients of dpa rate in ion irradiations, the injection of ions, and the physical discontinuity at the surface may introduce three new modes of segregation that probably affect precipitation behavior. Ultimately, these segregation processes may synergistically influence swelling through interaction with other neutron-atypical processes, especially the strong influence of dpa rate differences and defect imbalance effects.

6. RADIATION RESPONSE OF STRUCTURALLY ENGINEERED T91*

The previous study on T91 provides a foundation on which to compare the radiation response of a structurally engineered variant of the F/M alloy. The main objective of this study is to answer the question: Does the superior radiation resistance of T91 ECAE maintain, with respect to its unprocessed variant, at ultra-high damage levels? Equipped with knowledge and proper techniques for performing and analyzing specimens after ultra-high damage level irradiations, an assessment of the microstructural evolution in T91 ECAE and its stability relative to an unprocessed T91 alloy can be made. In order to provide the most cogent comparison, T91 and T91 ECAE were subject to the same conditions to minimize potential variations in the resulting microstructure.

6.1 Experimental Procedure

The heat of alloy T91 used in this study contained 9.4 wt% Cr and major alloying elements Mo, V, Si, Ni and Nb, with compositional details given in Table 5.1. The T91 was normalized at 1038°C for 0.5 h, followed by tempering at 760 °C for 0.5 h, with the specimen cooled in air after each step in the heat treatment [27]. ECAE processing was used for the severe deformation of T91. A fully tempered T91 bar was extruded at 300 °C for two passes with 90 degree rotations between each pass. Additional details on the technique can be found elsewhere [27,110]. The resulting material was cut into 4 mm × 2 mm plates and mechanically ground to a thickness of 0.5 mm using SiC grit paper of 600, 800, and 1200 grit. Mechanical polishing using a 0.05 um alumina solution and

*Reprinted with permission from "Radiation instability of equal channel angular extruded T91 at ultra-high damage levels", Jonathan G. Gigax, Hyosim Kim, Tianyi Chen, Frank A. Garner, and Lin Shao, Acta Materialia 132 (2017) pp. 395-404, Copyright 2017 by Elsevier.

followed by electropolishing was used to remove the surface damage introduced by the grinding step. Irradiation conditions were identical to those conditions used in the unprocessed T91 irradiation. Post-irradiation characterization utilized identical equipment in the study of the previous section.

To calculate grain boundary misorientation, more than 30 grains in each system were sampled resulting in more than 40 grain boundaries characterized. Although more grains were measured, larger grains located partially in the irradiated region with the remainder in the unirradiated region were not considered. Bright-field TEM and diffraction patterns were utilized to obtain an orientation map of the grains in the irradiated region (<1.5 um below the surface). The use of SEM electron backscatter diffraction was not chosen due to the heavy surface sputtering observed after irradiation.

6.2 Void Swelling

Figs. 6.1(a-c) show typical STEM micrographs obtained from coarse-grained T91 irradiated to 250, 750, and 1000 peak dpa, respectively. Figs. 6.1(d-f) show typical STEM micrographs obtained from extruded T91 irradiated to 250, 750, and 1000 peak dpa, respectively. At first glance, both coarse-grained (unextruded) and fine-grained (extruded) specimens appeared to behave similarly under ion irradiation. For the specimens irradiated to 250 peak dpa, voids developed heterogeneously through the specimens and were found predominantly near the ion-incident surface. With increasing damage level to 750 peak dpa, both void density and size increased, featuring similar heterogeneity as seen in the 250 peak dpa specimen. At 1000 peak dpa, voids moved deeper into the specimen. At this damage level, voids were more homogeneously distributed in both alloy variants.

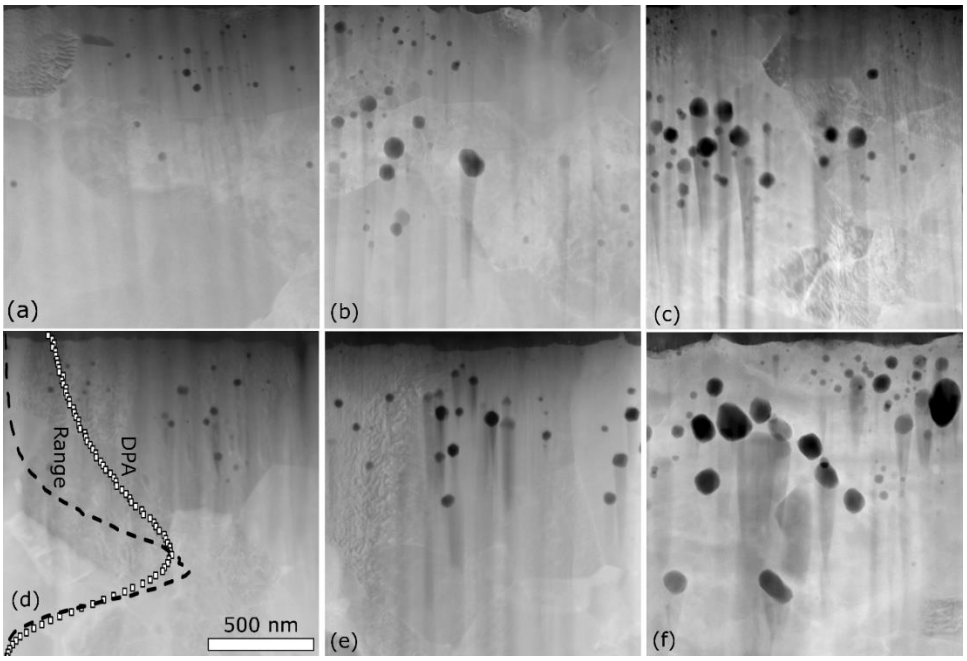

Figure 6.1 – Typical STEM-HAADF micrographs of coarse-grained T91 irradiated to peak dpa of 250 (a), 750 (b), and 1000 (c) and extruded T91 irradiated to peak dpa of 250 (d), 750 (e), and 1000 (f). SRIM ion range and damage profiles are superimposed in (d). Reprinted with permission from [109] Copyright 2017 by Elsevier.

Despite similar characteristics, a closer look reveals distinctly different swelling behaviors in the fine and coarse-grained specimens. Void distributions were more heterogeneous in the fine-grained T91with a lower overall void density but larger void swelling at 250 dpa. This heterogeneity is also seen at 750 peak dpa with the extruded T91 specimen exhibiting a significantly larger void growth than the control T91. At 1000 peak dpa, both coarse-grained T91 and extruded T91 exhibited more homogeneous void swelling, but the fine-grained T91 exhibited larger average void radius and shallower void distributions compared with the coarse-grained T91.

Fig. 6.2a provides the void swelling distribution as a function of depth for the coarse-grained T91 [74]. Void swelling at 250 peak dpa is confined to a depth region less than 400 nm and reached ~1% swelling. With increasing dose to 750 peak dpa, more significant swelling up to a maximum of ~6% developed and voids were found

within a depth of 1000 nm. At 1000 peak dpa, the swelling increased significantly with a maximum swelling of ~22% located at a depth of 500 nm, with voids observed to a depth of 1000 nm.

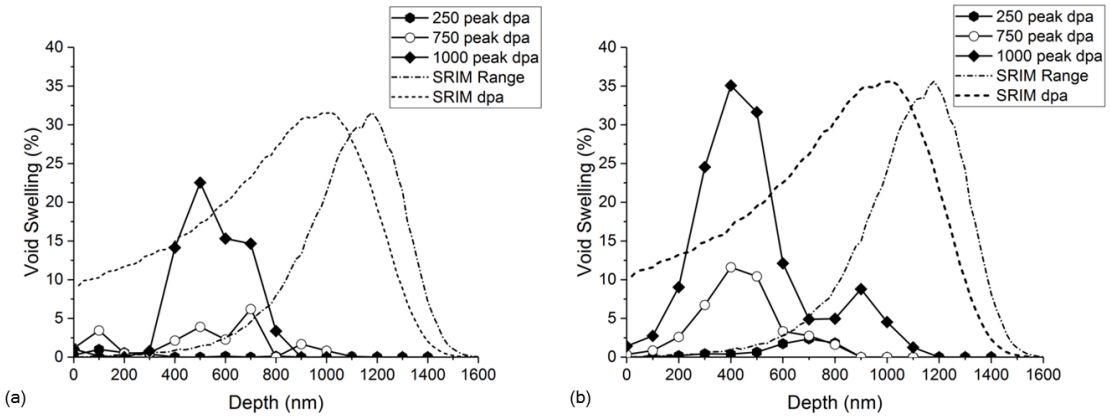

Figure 6.2 - Void swelling as a function of depth for both (a) coarse-grained and (b) extruded T91 specimens irradiated to a peak dpa of 250, 750, and 1000. SRIM dpa and Fe implant profiles are plotted for comparison. Reprinted with permission from [109] Copyright 2017 by Elsevier.

Fig. 6.2b shows the void swelling distribution in the extruded T91. At the lowest damage level, the peak swelling reaches a value of 2.5% at depths between 600 to 800 nm. At 750 peak dpa, significant swelling occurs between 200 and 600 nm, with a maximum swelling of ~13% between 400 and 600 nm. At 1000 peak dpa, the void swelling increases to a maximum value of ~37% at ~400 nm. Swelling is greatly suppressed in the peak dpa region and no void swelling is observed at the ion projected range, with an exception at 1000 peak dpa in the extruded T91 where a few voids are observed near the end of ion range. Although this observation may suggest that voids are beginning to form in the region at the end of ion range, we note that the static ion distribution predicted by SRIM that does not account for the changing density of the

material along the ion path, among several other factors [69]. Correcting for such changes to the density shifts the void swelling distribution towards the surface.

The void swelling distribution can be understood by several underlying phenomena. The first is the concept of "defect imbalance", which arises from a combination of the effects of forward recoil of target atoms and injection of extra atoms from implantation [61]. Since momentum transfer is along the forward directions, the depth profile of vacancies is slightly shallower than that of interstitials. Void formation is promoted at shallow depths due to excessive vacancies, but is greatly suppressed in the peak damage region due to excess interstitials. Considering the surface defect sink property for vacancy removal, the maximum swelling typically occurs at approximately half of the projected range of Fe implants [61].

Fig. 6.3a compares void swelling profiles of both coarse-grained T91 and extruded T91 irradiated to 1000 peak dpa. Fig. 6.3b compares their local swelling values taken from the depth from 300 to 500 nm. Note that the dpa values in Fig. 6.3b correspond to local dpa. We selected this depth region since it is less affected by both the surface and injected interstitial effects. The maximum swelling in extruded T91, observed at about 400 nm, is ~1.6 times greater than that of control T91, observed at about 500 nm. Furthermore, significant swelling of extruded T91 extends about 300 nm deeper than the control T91.

Fig. 6.3b shows two notable features in the depth region selected. First, the swelling rate estimated from the last two dose points in extruded T91 and coarse-grained T91 are 0.18%/dpa and 0.09%/dpa, respectively. Previous studies have shown that the neutron-induced steady-state swelling rate is about 0.2%/dpa for ferrite systems [10,11]. Similar swelling rates have been reached for some alloys using ion bombardment [74, 89,102,103]. Fig. 6.3b suggests that the extruded T91 exhibited steady state swelling. However, the control T91 did not yet reach this stage at the current damage levels. It can be concluded that the incubation swelling period of the extruded T91 is shorter than the coarse-grained T91.

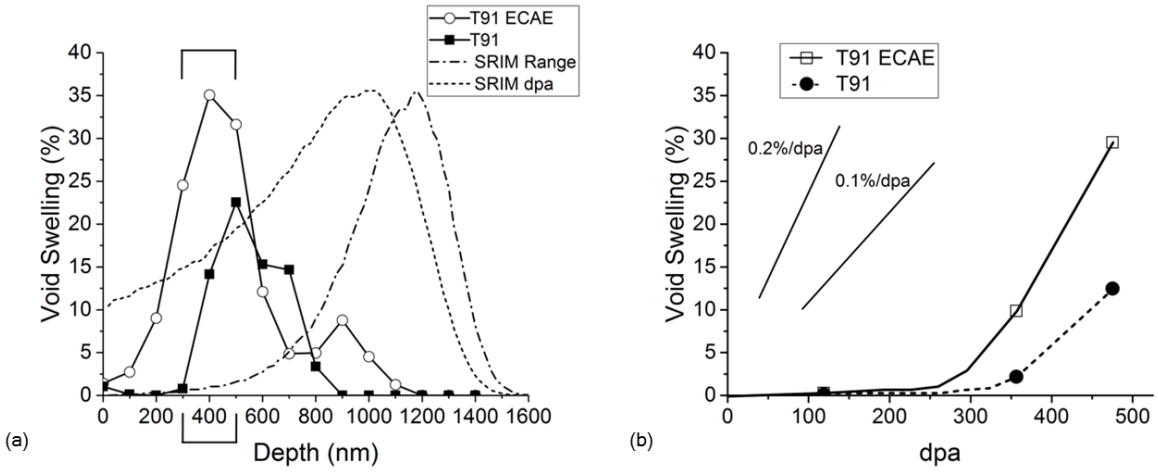

Figure 6.3 - (a) Measured void swelling profile as a function of depth for T91 and T91 ECAE at 1000 peak dpa, and (b) local void swelling measured from 300 nm to 500 nm (marked by brackets in (a)) for T91 and T91 ECAE at 250, 750, and 1000 peak dpa, respectively. SRIM ion range and damage curves are plotted in (a) for reference. Reprinted with permission from [109] Copyright 2017 by Elsevier.

Figs. 6.4(a-c) show typical bright-field TEM micrographs of extruded T91 after irradiation to 250, 750, and 1000 peak dpa, respectively, with grain boundaries marked by dashed lines. Void denuding near grain boundaries is observed for damage levels less than 1000 peak dpa. As shown in Fig. 6.4a and b, the average distances of voids to their nearest grain boundaries decrease with increasing damage level. At 1000 peak dpa, voids appear to intersect grain boundaries (Fig. 6.4c). Since large voids are immobile, it is assumed that the grain boundaries have moved to intersect the voids.

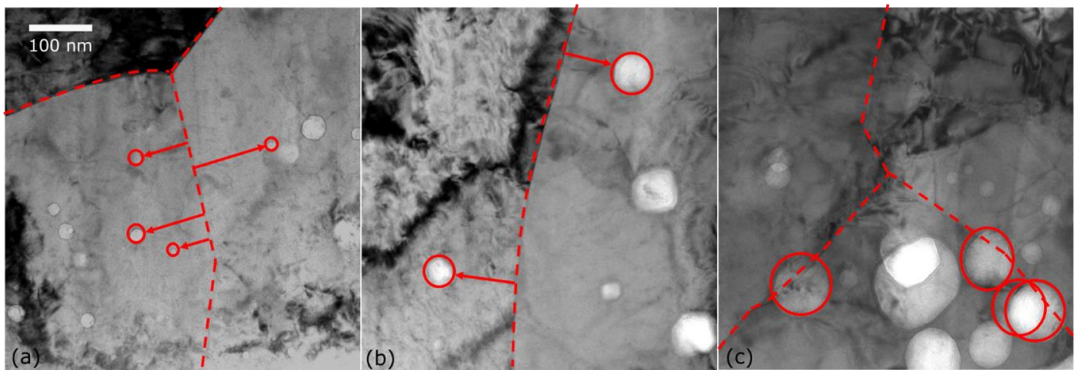

Figure 6.4 – Typical TEM bright field micrographs of select regions outlining the grain boundaries (dashed red outline) of T91 ECAE irradiated to damage levels of (a) 250, (b) 750, and (c) 1000 peak dpa, respectively. Reprinted with permission from [109] Copyright 2017 by Elsevier.

Earlier studies have shown that severely-deformed alloys have better radiation tolerance, often reflected by suppressed void swelling [27,89,111]. The mechanism was explained in numerous modeling studies by the defect sink properties of grain boundaries, notably through the production of a void denuded zone near grain boundaries. The present study, however, shows that the swelling resistance of severely deformed T91 is contrary to previous observations. That is, the deformed alloys have higher swelling despite the final grain sizes after coarsening remaining smaller than those in the control samples. The results of the experiment provide evidence that new mechanisms are needed to explain this discrepancy.

Fig. 6.5 provides a comparison of T91 irradiated in this study and dual-phase EP-450 and fully martensitic HT9 irradiated at the ESUV-1 facility at the Kharkov Institute of Physics and Technology [102,103]. Swelling values for control T91 and extruded T91 are taken from a depth region between 300 nm and 500 nm, corresponding to local values of 120, 360, and 475 dpa, respectively. Swelling data for EP-450 and HT9 are taken from a depth interval 100-200 nm below the ion-incident surface. There are several notable observations in this comparison. First, the incubation periods for swelling in extruded and coarse-grained variants of T91 are larger than the ferrite phase

in EP-450. The lack of higher swelling data for tempered martensite in EP-450 precludes a fair comparison against T91 and HT9. However, the available data suggests that the incubation period for tempered martensite in EP-450 is lower than that of T91 and HT9. The steady-state swelling rate of extruded T91 closely matches that of cold-worked HT9.

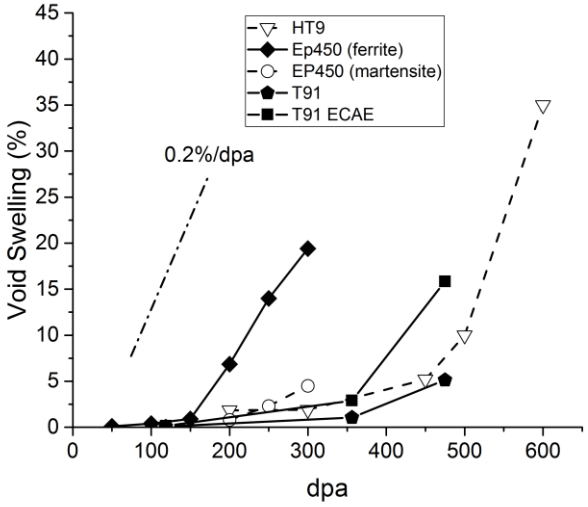

Figure 6.5 – Comparison of swelling in T91 observed in this study with swelling observed in previous studies on HT9 and EP-450 [102,103]. Reprinted with permission from [109] Copyright 2017 by Elsevier.

Fig. 6.6 compares the swelling in the region of 200-500 nm of the present study with that observed in various neutron irradiation experiments [71,82-85]. Note that all ion-induced swelling points in Fig. 6.6 are plotted as a function of local dpa. The low dose swelling behavior in both ion irradiated T91 specimens is similar to that of the neutron irradiation data. Ion irradiation at high dpa rates appears to slightly delay the onset of swelling compared to that under neutron irradiation, suggesting a dependence of the duration of the transient swelling regime on dpa rate.

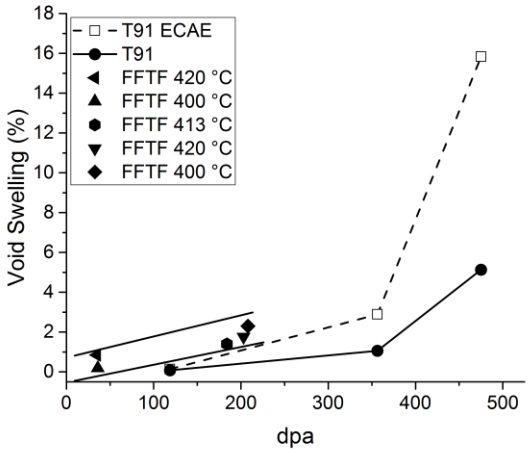

Figure 6.6 – A comparison between the swelling behavior of various heats of T91 irradiated in the Fast Flux Test Facility (FFTF) [71,82-85] and ion-irradiated variants of T91 from this study (data taken from a depth interval of 200-500 nm). Reprinted with permission from [109] Copyright 2017 by Elsevier.

6.3 Grain Evolution

Grain coarsening is an important structural evolution accompanying void swelling in this study. Figs. 6.7(a-d) provide a cross-sectional STEM image comparison of extruded T91 with increasing dpa values. Prior to irradiation, grains are equiaxed and have an average size of ~300 nm. Irradiation to 250, 750, and 1000 peak dpa produces a large degree of anisotropic grain growth, with grains growing preferentially along the ion incident direction. The growth results in the formation of columnar-like grains spanning an average size of at least 500 nm and, in some cases, up to a maximum of ~1000 nm. The lower dashed line in Fig. 6.7 marks the projected range of 3.5 MeV Fe ions. Significant grain growth occurs only within the irradiated region.

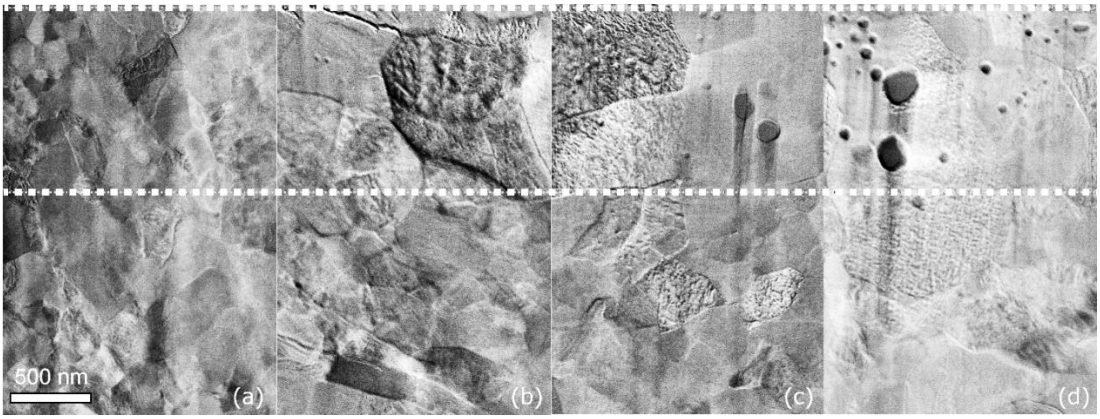

Figure 6.7 – Typical STEM images of an (a) unirradiated specimen, and specimens irradiated to (b) 250, (c) 750 peak dpa, (d) and 1000 peak dpa. The ion irradiated region is enclosed by dashed white lines. Reprinted with permission from [109] Copyright 2017 by Elsevier.

In order to separate annealing effects from radiation effects, we analyzed the grain size changes in both the irradiated region and beyond the irradiated region to separate thermal annealing effects from radiation-induced effects. The dpa dependence of grain growth is plotted in Fig. 6.8. The comparison between the irradiated region and unirradiated region shows that the grain growth of the irradiated region has two distinct inflection points at which the grain growth rates increase. One increase appeared at ~250 peak dpa, with another occurring at a much higher dose (>750 peak dpa). By comparison, grain size changes in the unirradiated region maintain a relatively low and constant growth rate, with the increase approaching ~25% at the highest damage levels compared to ~175% for the irradiated region. The unirradiated region is free from radiation damage and grain evolution is driven by thermal annealing only. Thus, the dramatic grain growth observed in the irradiated region is enhanced significantly by athermal processes.

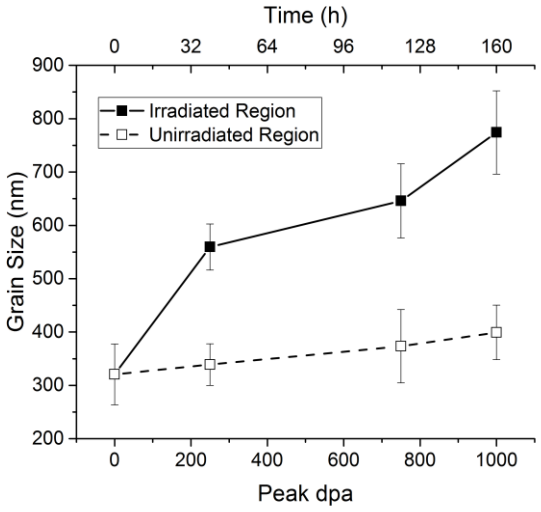

Figure 6.8 - Average grain size of irradiated T91 ECAE as a function of damage level for the irradiated and unirradiated regions. The unirradiated region refers to depths well beyond the projected ion range. Reprinted with permission from [109] Copyright 2017 by Elsevier.

Irradiation studies on deformed ferritic-martensitic alloys have shown comparatively good grain stability during thermal annealing [27,89,111]. Under irradiation, however, several studies on various nano-grained specimens, primarily pure metals, have reported large grain growth after irradiation [29-32]. In the grain growth model proposed by Kaoumi et al., grain growth occurs when thermal spikes from damage cascades, produced by collision atoms near grain boundaries, thermally excite atoms locally [32]. The net direction of atom migration is determined by the driving forces for grain growth (e.g. grain boundary curvature, solute concentration gradients), which leads to a net curvature reduction in the grain boundary, thereby driving grain growth.

The thermal spike model may describe the grain evolution at low doses in our system. The athermal grain growth mechanism in this model requires damage cascade creation near grain boundaries. For small grains, the likelihood of a damage cascade near grain boundaries is high and is coupled with a strong driving force for grain growth via grain boundary curvature reduction. With increasing grain sizes, this effect becomes

weaker. The thermal spike model, however, cannot explain the rapid growth at damage levels beyond 750 peak dpa, an observation that must involve a different athermal mechanism.

In order to understand the source of the increasing grain growth rate beyond 750 peak dpa, we examined the grain size changes in the coarse-grained T91 as well. Fig. 6.9 compares the average grain size in the irradiated regions of both coarse and fine-grained T91. At low doses from 0 to 250 peak dpa, the grain size in coarse-grained T91 does not exhibit similar grain size growth as observed in the extruded T91. Both specimens, however, exhibit rapid growth beyond 750 peak dpa. The similarity in grain growth suggests that the mechanism responsible is independent of grain size. Instead, the increase in grain size occurring at 750 peak dpa correlates to a common change in the microstructure: void swelling. Fig. 6.3b shows that around 750 peak dpa, both the coarse and fine-grained samples exhibited a large increase in the swelling rate (at a depth between 300-500 nm, corresponding to a 360 local dpa), with the void swelling increasing by an additional ~9% and ~18% from 750 to 1000 peak dpa (360 to 475 local dpa), respectively. The potential coupling of grain growth and void swelling is further examined in the discussion section.

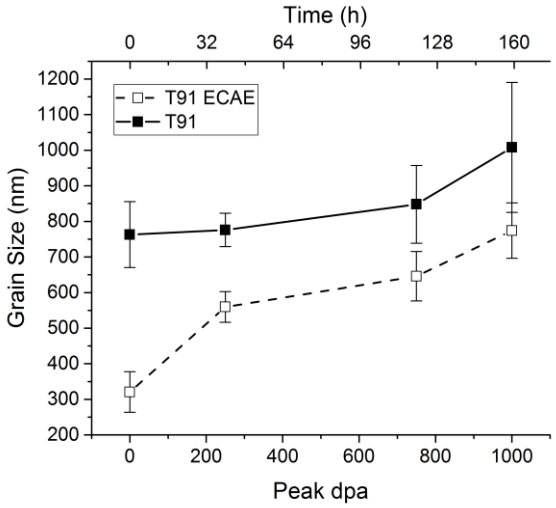

Figure 6.9 - Average grain sizes of irradiated coarse-grained and extruded T91 as a function of peak damage level. Data are taken only from the irradiated regions. Reprinted with permission from [109] Copyright 2017 by Elsevier.

6.4 Radiation-induced Precipitation

Fig. 6.10 shows EFTEM images of coarse-grained and fine-grained T91 with grain boundaries and precipitates annotated in the figure. A Cr jump map was chosen to show the difference in solute concentrations between the fine and coarse grain samples at 250 peak dpa. Mn, Ni, and Cu jump maps were also obtained to verify solute behavior. After irradiation to 250 peak dpa, T91 shows the precipitation of Cr-rich precipitates in grains, with a few located on grain boundaries. These precipitates appear throughout the irradiated region but do not appear beyond the ion range, indicating that the precipitation results from irradiation.

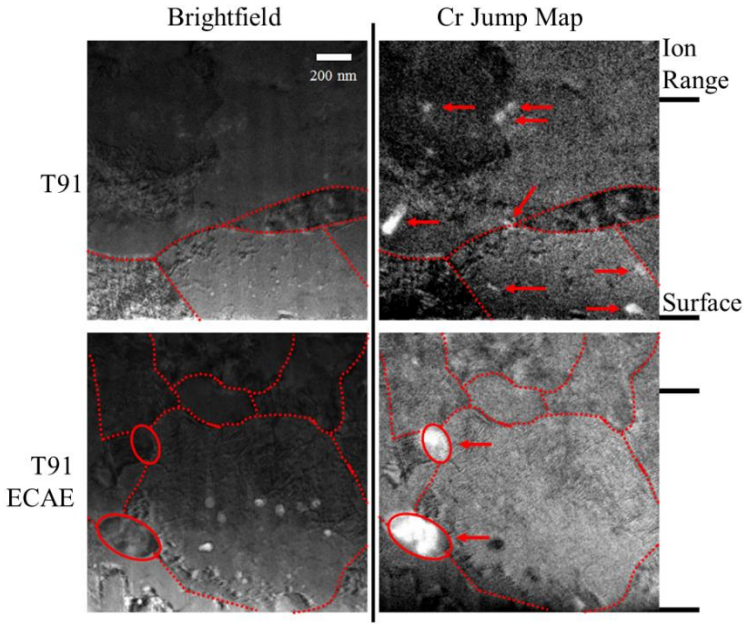

Figure 6.10 – Typical bright field and energy filtered TEM micrographs of select regions in coarse-grained and extruded T91 irradiated to 250 peak dpa. Grain boundaries are marked by dashed lines and solutes are encircled by solid lines. Arrows indicate Cr-rich precipitates in the Cr jump map. Reprinted with permission from [109] Copyright 2017 by Elsevier.

A comparison to the fine-grained T91 reveals a striking difference. The Cr-rich precipitates are only observed on grain boundaries with no presence within grains, suggesting that solutes are largely depleted within grains. Furthermore, the Cr-rich precipitates are larger in size than those in coarse-grained T91. These observations are not unexpected as the ECAE process relies heavily on the formation of precipitates to pin dislocations and grain boundaries to produce a fine grain structure. We note that the lack of radiation-induced precipitation in nano-grained specimens was also observed in fine-grained SS304 subject to similar ECAE processing and heavy ion irradiation [111].

6.5 Correlation of Void Swelling and Grain Growth

The void swelling behavior at high doses of the coarse-grained and extruded T91 differs greatly from much of the lower dose irradiations in fine-grained systems studied to date. We attribute some of these differences to several possible phenomena. First, T91 contains a number of minor solutes that have been added to achieve a range of desired properties. These solutes have been observed to influence the void swelling behavior of steels, serving to suppress void swelling at low doses [16,19]. For severe deformation processes, interstitial solutes play a key role in achieving a fine grain structure [112]. Large solute-rich precipitates were observed on grain boundaries of the extruded T91 with densities higher than that of the control sample. This solute precipitation is expected to alter the microscopic composition within grains. Since both variants have similar compositions, the lower concentration of solutes within grains of the extruded T91 compared to the unprocessed variant suggests that the different void swelling behaviors may arise from this difference.

Second, previous studies showed that cold-working promoted swelling at elevated temperatures for some soft alloys that had difficulty establishing a stable radiation-induced dislocation network, with cold-working and subsequent thermal aging producing even larger increases in void swelling [6,10]. The effect is present at two stages. Prior to irradiation, the dislocation network from cold-working promotes void nucleation in dislocation-free regions through biased interstitial absorption. The onset of steady-state void swelling observed at higher damage levels is accompanied by the production of a dense dislocation network. The movement and subsequent pile-up of dislocations at grain boundaries at these doses act as a biased defect sink for interstitials and the effect further compounds on the pre-existing interstitial defect biases. Cold-working does not appear to influence the steady-state swelling rate significantly, implying the strongest effect is on the incubation period of swelling. The swelling rate for extruded T91 nearly reaches the 0.2%/dpa steady-state swelling rate expected for bcc F/M alloys, while the coarse-grained T91 has reached only half of the steady-state rate.

The fact that the control T91 does not reach the expected steady state swelling rate suggests that it is still in its transient swelling stage. From Fig. 3b, the incubation period for attaining the steady-state swelling is ~100 dpa less for the extruded T91 than the coarse-grained T91.

It is important to note that creep may also play a role in the observed void swelling behavior. It is well known that void swelling can enhance creep through biased defect migration towards different defect sinks: vacancies to voids and interstitials to dislocations [113]. The present study shows different but similar biased defect-sink interactions: vacancies to voids and interstitials to growing grain boundaries. Both the current and previous study showcase the complexity of correlated microstructural evolution under extreme radiation conditions.

The previously discussed phenomena do not address the grain instability in T91 ECAE and its impact on void swelling. Our discussion focuses on the following phenomena, followed by our hypothesis and explanation:

1) Although the grain sizes in extruded T91 are smaller than the grains in coarse-grained T91 at all doses, extruded T91 has higher swelling than control T91. This cannot be explained by a simple treatment of boundary sink strength, which is proportional to 1/d, where d is the grain diameter [114]. The discrepancy suggests that additional complexity from grain boundary structural changes must be considered.
2) At peak dpa >750, rapid grain growth starts for both coarse and fine-grained T91. At the same damage levels, more rapid void swelling starts for both specimens. The rapid grain growth at high damage level is closely correlated to swelling, regardless of the grain sizes.

The grain instability observed in this study is accompanied with a significant reduction in the sink strength or sink neutrality of the growing grain boundaries in the irradiated region due to a combination of the lowering of the grain boundary misorientation angles and the buildup of defects on the grain boundary itself. Fig. 6.11 plots the misorientation angles of grains in unirradiated T91 ECAE and T91 ECAE

irradiated to 250 peak dpa. Both specimens are populated with a larger fraction of low angle grain boundaries than high angle grain boundaries. However, the low angle grain boundary fraction appears to enrich after irradiation to 250 peak dpa with an accompanying drop in high angle grain boundaries. The average misorientation angle measured after 250 peak dpa was found to be ~11°. The ratio of low angle to high angle grain boundaries was found to be 2 in the irradiated region. By comparison, the average misorientation angle in the unirradiated specimen is measured to be ~17° with a ratio of only ~1.2. It is important to note that low angle grain boundaries are typically characterized by a collection of dislocations, while high angle grain boundaries feature a unique atomic structure from the matrix [115,116]. Careful attention must be paid with regards to the grain boundary structure as the sink strength shows a large disparity between different misorientation angles and grain boundary types [26,117,118]. Chen *et al*. showed that when the misorientation angle becomes lower, the areal density of defect formation energy minima on a grain boundary is reduced, leading to reduced defect loading paths. This results in lower sink strength for low angle grain boundaries compared to high angle boundaries, suggesting that the overall sink strength of the grain boundaries in the irradiated system decreases from structural changes.

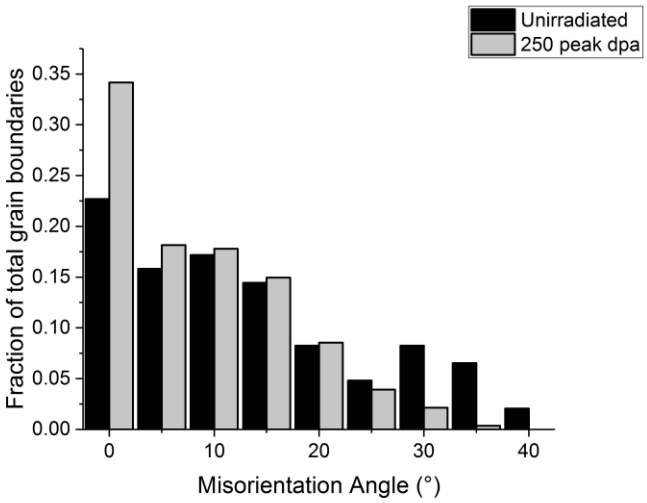

Figure 6.11 – Misorientation angle distribution measured in the unirradiated fine-grained T91 and extruded T91 irradiated to 250 peak dpa. Misorientation angles averaged into 5° bins. Reprinted with permission from [109] Copyright 2017 by Elsevier.

For the grain growth at a high damage level (>750 peak dpa), a new mechanism is needed to explain the correlation with void swelling. Significant void growth results from void nucleation and subsequent net vacancy absorption. Based on a simple argument involving point defect balance, a biased interstitial flux towards grain boundaries must exist. Although grain boundaries are often treated as neutral defect sinks for both interstitials and vacancies, nothing is known about a growing grain boundary. Previous studies suggest the possibility of a changing defect bias for a grain boundary under irradiation [21,119-123]. A recent study by Dey *et al.* showed irradiation can induce grain growth in nanocrystalline zirconia, and that grain growth cannot be avoided even with adding dopants to grain boundaries to reduce boundary energies [124]. It was argued by Dey *et al*. that a growth mechanism different from thermally activated boundary movement must be involved under heavy ion irradiation and that a reduction in grain boundary energy leads to a lower grain boundary sink strength. This is in agreement with the results in the present study showing the complexity of grain boundary sink property changes. The experimental evidence

presented suggests that the defect sink property of a growing boundary is different from that of a static grain boundary. Since the correlation of grain growth and void swelling is observed in both extruded T91 and coarse grain T91, the biased defect sink property must occur independently of both grain boundary densities and boundary misorientation angles.

The major microstructural changes that occur in the fine-grained T91 are illustrated in Fig. 6.12 and can be summarized as follows:

1) At low doses, ion irradiation produces defects that are removed efficiently by the dense grain boundaries shown in Fig. 6.12a. However, the grains are observed to grow significantly, with grain boundaries undergoing structural changes arising from both grain growth and defect loading.
2) Additional irradiation to higher doses (750 peak dpa) results in the formation of voids, a complex dislocation network that piles up near grain boundaries at the end of ion range, and slight increases to grain size (Fig. 6.12b). Due to the defect imbalance effect, the near surface regions are vacancy-rich while the deeper depths near the end of ion range are interstitial-rich, leading to the appearance of small voids in the near surface region. The grain growth at lower doses is correlated to significantly more swelling in the fine-grained T91 than in the coarse-grained counterpart, with this behavior continuing to higher doses.
3) A second large increase in grain size is observed at ultra-high doses of 1000 peak dpa (Fig. 6.12c). Significant void swelling was observed for both fine and coarse-grained T91, with the fine-grained specimen approaching the expected steady-state swelling rate of bcc steels. The correlated increase in void swelling and grain growth, observed in both fine and coarse-grained T91, arises primarily from voids acting as biased vacancy defect sinks, resulting in a large interstitial flux to the growing grain boundaries.

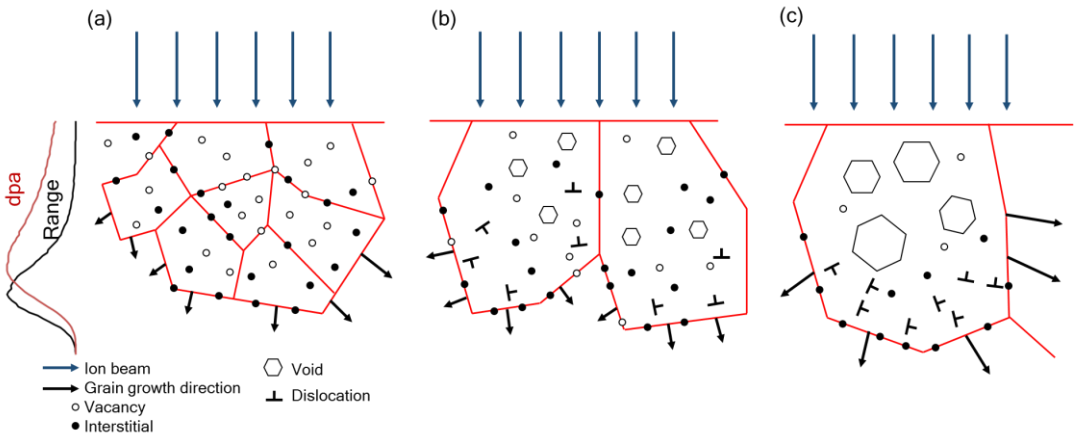

Figure 6.12 – Illustration of the microstructural evolution of extruded T91 irradiated to (a) 250, (b) 750, and (c) 1000 peak dpa. Reprinted with permission from [109] Copyright 2017 by Elsevier.

The present study points to the importance of ultra-high dpa testing of candidate alloys. Conclusions from low dpa testing cannot be extended to high dpa performance when features introduced by composition engineering or structural engineering may evolve under ion irradiation. The study also shows that grain boundary density is not the only parameter determining the defect removal capability of boundaries, but also by other important factors such as the misorientation angle. It is beyond the scope of the present study to explain how a growing grain boundary can absorb interstitials as a biased sink, or how a biased interstitial loading can promote grain growth. Additional atomic scale modelling is needed to reveal the fundamental processes.

7. CONCLUSIONS

In the present work, three effects that operate strongly on the void swelling response of the system were investigated. Defect imbalance is an intrinsic phenomenon that arises from the use of an ion to introduce damage in the system. The irradiation revealed that voids form between the surface and the end of the implanted ion range. Future void swelling analysis should then focus on this region. The effect of rastering or pulsing an ion beam was shown to dramatically suppress swelling with increasing rastering speed. Since the swelling rate from the static, defocused beam best matched the expected 0.2%/dpa stead-state swelling rate, a static beam is strongly recommended for neutron simulation of damage. Third, it was observed that without filtering techniques ion irradiated HT9 developed carbides and an elevated carbon concentration in the near surface region after irradiation. This was found to suppress swelling dramatically. After employing a filtering system, the carbon in the near surface was found to be similar to the unirradited sample and void swelling better matched neutron swelling behavior in HT9. By addressing each of these neutron-atypical effects, the impact these have on the microstructural evolution under irradiation can be minimized enabling a more meaningful exploration of irradiation effects at high damage levels.

In addition to the studies on neutron atypical effects, two studies investigating the response of a compositionally engineered material, T91, and its structurally engineered variant were performed. The results show that T91 behaves similarly to the low damage level neutron behavior and possess good swelling resistance. However, the structurally engineered variant possessed poorer swelling resistance than its unprocessed counterpart, developing more severe microstructural changes at ultra-high damage levels. This is in direct contrast to previously published low damage level studies, implying the importance of high damage level irradiations to fully understand microstructural evolution under irradiation.

REFERENCES

1. F. A. Garner, Chapter 6: "Irradiation Performance of Cladding and Structural Steels in Liquid Metal Reactors," Vol. 10A of Materials Science and Technology: A Comprehensive Treatment, VCH Publishers, 1994, pp. 419-543.

2. F.A. Garner, "Radiation Damage in Austenitic Steels", in Konings, R.J.M., (ed.) Comprehensive Nuclear Materials, Volume 4, (2012) pp. 33-95, Elsevier.

3. F. A. Garner, Recent insights on the swelling and creep of irradiated austenitic alloys, J. Nucl. Mater. 122-123 (1984) 459-471.

4. F. A. Garner and H. R. Brager, Swelling of austenitic iron-nickel-chromium ternary alloys during fast neutron irradiation, Effects of Radiation on Materials: Twelfth International Symposium, ASTM STP 870, ASTM, Philadelphia, PA, 1985, pp. 187-201.

5. F. A. Garner and A. S. Kumar, Effects of Radiation on Materials: Thirteenth International Symposium (Part 1) Radiation-Induced Changes in Microstructure, ASTM STP 955, ASTM, Philadelphia, PA, 1987, pp. 289-314.

6. F. A. Garner, C. A. Black and D. J. Edwards, Factors which control the swelling of Fe-Cr-Ni ternary austenitic alloys, J. Nucl. Mater. 245 (1997) 124-130.

7. M. L. Hamilton, F. H. Huang, W. J. S. Yang and F. A. Garner, Effects of Radiation on Materials: Thirteenth International Symposium (Part II) Influence of Radiation on Material Properties, ASTM STP 956, ASTM Philadelphia, PA, 1987, pp. 245-270.

8. V. S. Neustroev and F. A. Garner, Very high swelling and embrittlement observed in a Fe-18Cr-10Ni-Ti hexagonal fuel wrapper irradiated in the BOR-60 fast reactor, J. Nucl. Mater. 378 (2008) 327-332.

9. S. I. Porollo, A. N. Vorobjev, Yu. V. Konobeev, A. M. Dvoriashin, V. M. Krigan, N. I. Budylkin, E. G. Mironova and F. A. Garner, Swelling and void-induced embrittlement of austenitic stainless steel irradiated to 73-82 dpa at 335-365 C, J. Nucl. Mater. 258-263 (1998) 1613-1617.

10. F. A. Garner, M. B. Toloczko and B. H. Sencer, Comparison of swelling and irradiation creep behavior of fcc-austenitic and bcc-ferritic/martensitic alloys at high neutron exposure, J. Nucl. Mater. 276 (2000) 123-142.

11. B. H. Sencer, F. A. Garner. Compositional and temperature dependence of void swelling in model Fe-Cr base alloys irradiated in the EBR-II fast reactor, J. Nucl. Mater. 283-287 (2000) 164.

12. G.R. Odette, On mechanisms controlling swelling in ferritic and martensitic alloys, J. Nucl. Mater. 155–157 (1988) 921.

13. Sniegowski, J.J. and W.G. Wolfer, Proc. of Topical Conference on Ferritic Alloys for use in Nuclear Energy Technologies. (Snowbird) (1983), 579-586.

14. R. Bullough, M.H. Wood, and E.A. Little, in Effects of Radiation on Materials: Tenth Conference, ASTM STP 725, pp. 593

15. E.A. Little, R. Bullough, and M.H. Wood, On the swelling resistance of ferritic steel, Proc. Roy. Soc. (London) A372 (1980) 565

16. Yu. V. Konobeev, A. M. Dvoriashin, S.I. Porollo, and F. A. Garner, Swelling and microstructure of pure Fe and Fe-Cr alloys after neutron irradiation to ~26 dpa at 400 C, J. Nucl. Mater. 355 (2006) 124-130.

17. E. A. Little, Void swelling in irons and ferritic steels: I. Mechanisms of swelling suppression, J. Nucl. Mater. 87 (1979) 11.

18. E.A. Little and D.A. Stow, Void swelling in irons and ferritic steels: II. An experimental survey of materials irradiated in a fast reactor, J. Nucl. Mater. 87 (1979) 25.

19. S.I. Porollo, A.M. Dvoriashin, A.N. Vorobjev, Yu.V. Konobeev, The microstructure and tensile properties of Fe-Cr alloys after neutron irradiation at 400 C to 5.5-7.1 dpa, J. Nucl. Mater. 256 (1998) 247.

20. D.S. Gelles, Fusion Reactor Materials Semiannual Progress Report, DOE/ER-0313/1 (1987) p. 145.

21. X. M. Bai, A. F. Voter, R. G. Hoagland, M. Nastasi, B. P. Uberuaga, Efficient annealing of radiation damage near grain boundaries via interstitial emission, Science 327 (2010) 1631–1634.

22. R.Z. Valiev, R.K. Islamgaliev, I.V. Alexandrov, Bulk nanostructured materials from severe plastic deformation, Prog. Mater. Sci. 45 (2000) 103.

23. Z. Y. Iwahashi, M. Horita, M. Nemoto, and T. G. Langdon, The process of grain refinement in equal-channel angular pressing, Acta Mater. 46 (1998) 3317–3331.

24. R. Valiev, Nanostructuring of metals by severe plastic deformation for advanced properties, Nat. Mater. 3, 511–516 (2004).

25. M. Dollar, H. Gleiter, Point-defect annihilation at grain boundaries in gold, Scr. Metall. 19 (1985) 481.

26. W.Z. Han, M.J. Demkowicz, E.G. Fu, Y.Q. Wang, and A. Misra, Effect of grain boundary character on sink efficiency, Acta Mater. 60, 6341 (2012).

27. M. Song, Y.D. Wu, D. Chen, X. M. Wang, C. Sun, K. Y. Yu, Y. Chen, L. Shao, Y. Yang, K. T. Hartwig, X. Zhang, Response of equal channel angular extrusion processed ultrafine-grained T91 steel subjected to high temperature heavy ion irradiation, Acta Materialia 74 (2014) 285–295.

28. B. H. Sencer and F. A. Garner, Compositional and temperature dependence of void swelling in model Fe-Cr base alloys irradiated in the EBR-II fast reactor, J. Nucl. Mater. 283-287 (2000) 164.

29. W. Han, E. G. Fu, M. J. Demkowicz, Y. Wang, and A. Misra, Nanograined copper under helium bombardment at 450 C, J. Mater. Res. 28 (2013) 2763-2770.

30. D. Kaoumi, A. T. Motta, and R. C. Birtcher, Grain growth in nanocrystalline metal thin films under in situ ion-beam irradiation, J. ASTM Inter. 4 (2007).

31. W. B. Liu, C. Zhang, Y. Z. Ji, Z. G. Yang, H. Zang, T. L. Shen, L. Q. Chen, Irradiation-induced grain growth in nanocrystalline reduced activation ferrite/martensite steel, App. Phys. Lett. 105 (2014) 121905.

32. D. Kaoumi, A. T. Motta, R. C. Birtcher, A thermal spike model of grain growth under irradiation, App. Phys. Lett. 104 (2008) 073525.

33. G. S. Was, Fundamentals of Radiation Materials Science: Metals and Alloys, Springer, New York, 2007.

34. L. R. Greenwood, Neutron interactions and atomic recoil spectra, J. Nucl. Mater. 216 (1994) 29.

35. L. Shao, X. Lu, X. Wang, L. Rusakova, J. Liu, W. K. Chu, Retardation of boron diffusion in silicon by defect engineering, Appl. Phys. Lett. 78 (2001) 2321.

36. F.A. Garner. Impact of the injected interstitial on the correlation of charged particle and neutron-induced radiation damage, J. Nucl. Mater. 117 (1983), 177-197.

37. F. A Garner, G. L. Guthrie, E. R. Gilbert, Radiation Effects and Tritium Technology for Fusion Reactors, CONF-750989, vol. 1, pp. 474-490.

38. F. A Garner, G. L. Guthrie, Radiation Effects and Tritium Technology for Fusion Reactors, CONF-750989, vol. 1, pp. 491-518.

39. W. G. Wolfer, F. A. Garner, J. Nucl. Mater. 583 (1979) 85-86.

40. V. K. Sethi, P. R. Okamoto, Conference on Phase Stability During Irradiation, The Metallurgical Society of AIME, Pittsburgh, PA, 1980, pp. 109-117.

41. J. Lindhard, V. Nielsen, M. Scharff, K. Dan, Vidensk. Selsk. Mat. Fys. Medd. 36 (1970) 1.

42. W. D. Wilson, L. G. Haggmark, J. P. Biersack, Phys. Rev. B 15 (1977) 2458.

43. L. Shao, Nucl. Instrum. Methods Phys. Rev. B 268 (2010) 3564.

44. J.F. Ziegler, M.D. Ziegler, J.P. Biersack, SRIM – the stopping range of ions in matter, Nucl. Instr. Methods Phys. Res. B 268 (2010) 1818–1823.

45. N. I. Budylkin, E. G. Mironova, V. M. Chernov, V. A. Krasnoselov, S. I. Porollo, F. A. Garner, Neutron-induced swelling and embrittlement of pure iron and pure nickel irradiated in the BN-350 and BOR-60 fast reactors, J. Nucl. Mater. 375 (2008) 359.

46. A. M. Dvoriashin, S. I. Porollo, Yu. V. Konobeev, F. A. Garner, Influence of cold work to increase swelling of pure iron irradiated in the BR-10 reactor to ~6 and ~25 dpa at 400 C, J. Nucl. Mater. 283-287 (2000) 157.

47. D. L. Plumton and W. G. Wolfer. Suppression of void nucleation by injected interstitials during heavy ion bombardment, J. Nucl. Mater. 120 (1984) 245-253.

48. E. H. Lee, L. K. Mansur, and M. H. Yoo. Spatial variation in void volume during charged particle bombardment – the effects of injected interstitials, J. Nucl. Mat. 85 & 86, 577 (1979).

49. D. L. Plumton, G. L. Kulcinski. The magnitude and distribution of the excess interstitial fraction during heavy ion bombardment, J. Nucl. Mat. 133 & 134, 444 (1985).

50. L. K. Mansur and M. H. Yoo. Advances in the theory of swelling in irradiated metals and alloys, J. Nucl. Mater. 85 & 86 (1979) 523-532.

51. D. B. Bullen, G. L. Kulcinski, and R. A. Dodd. Swelling suppression by injected self-interstitials, Nucl. Instr. Meth. Phys. Res. B 10/11 (1985) 561-564.

52. J. B. Whitley, G. L. Kulcinski, P. Wilkes, H. V. Smith Jr. The depth dependent damage profile in nickel irradiated with nickel or copper ions, J. Nucl. Mater. 79 (1979) 159-169.

53. D. L. Plumton, H. Attaya, W. G. Wolfer. Conditions for the suppression of void formation during ion-bombardment, J. Nucl Mater. 122 & 123 (1984) 650-653.

54. A. D. Brailsford and L. K. Mansur. Effect of self-ion injection in simulation studies of void swelling, J. Nucl. Mater. 71 (1977) 110-116.

55. ASTM E521, 2009, "Standard Practice for Neutron Radiation Damage Simulation by Charged-Particle Irradiation," ASTM International, West Conshohocken, PA, DOI: 10.1520/E0521-96R09E01, www.astm.org

56. J. A. Sprague, F. A. Smidt, Jr., J. E. Westmoreland and P. R. Malmberg, NRL Memorandum 2555 (1972).

57. J. A. Sprague and F. A. Smidt. NRL Memorandum 2692 (1972).

58. A. Taylor, D.I. Potter, and H. Wiedersich. ANL/CTR/TM-39, Argonne National Laboratory (1975).

59. R. E. Stoller, M. B. Toloczko, G. S. Was, A. G. Certain, S. Dwaraknath, and F. A. Garner. On the use of SRIM for computing radiation damage exposure, Nucl. Instr. Meth. Phys. Res. B 310 (2013), 75-80.

60. G. Wulff. Zeitschrift fur Krystallographie und Mineralogie. 34 (1901) 449-530.

61. L. Shao, C.-C. Wei, J. Gigax , A. Aitkaliyeva, D. Chen, B. H. Sencer, F. A Garner. Effect of defect imbalance on void swelling distributions produced in pure iron by 3.5 MeV self-ions, J. Nucl. Mater. 453 (2014) 176-181.

62. E. Kuramoto, N. Yoshida, N. Tsukuda, K. Kitajima, N. H. Packan, M. B. Lewis, L. K. Mansur, Simulation irradiation studies on iron, J. Nucl. Mater. 103 (1981) 1091-1096.

63. N. Ghoniem and G. L. Kulcinski. Swelling of metals during pulsed irradiation, J. Nucl. Mater. 69-70 (1978) 816-820.

64. E. P. Simonen, N. M. Ghoniem, and H. K. Packan. Pulsed flux effects on radiation damage, J. Nucl. Mater. 122 & 123 (1984) 391-401.

65. E. Getto, Z. Jiao, A.M. Monterrosa, K. Sun, G.S. Was, Effect of irradiation mode on the microstructure of self-ion irradiated ferritic-martensitic alloys, J. Nucl. Mater. 465 (2015) 116-126.

66. J. G. Gigax, E. Aydogan, T. Chen, D. Chen, L. Shao, Y. Wu, W. Y. lo, Y. Yang, F. A. Garner, The influence of ion beam rastering on the swelling of self-ion irradiated pure iron at 450 C, J. Nucl. Mater. 465 (2015) 343-348.

67. V.A. Pechenkin , A.D. Chernova and, F.A. Garner, Proceedings of Accelerator Applications, 2013, Bruges, Belgium.

68. K. Vörtler, L. Barnard, I. Szlufarska, D. Morgan, F. A. Garner, J. Nucl. Mater. 479 (2016) 23-35.

69. J. Wang, M. B. Toloczko, N. Bailey, F. A. Garner, J. Gigax, L. Shao, Modification of SRIM-calculated dose and injected ion profiles due to sputtering, injected ion buildup and void swelling, Nucl. Instr. Meth. Phys. Res. B 387 (2016) 20–28.

70. L. Shao, J. G. Gigax, D. Chen, H. Kim, F. A. Garner, J. Wang, M. B. Toloczko, Nucl. Instr. Meth. Phys. Res. B., *in press.*

71. M. B. Toloczko, F. A. Garner, and C. R. Eiholzer, Irradiation creep and swelling of the US fusion heats of HT9 and 9Cr-1Mo to 208 dpa at 400 C, J. Nucl. Mater., 212-215 (1994) 604-607.

72. M. B. Toloczko and F. A. Garner, Irradiation creep and void swelling of two LMR heats of HT9 at ~400 C and 165 dpa, J. Nucl. Mater., 233-237 (1996) 289-292.

73. B. H. Sencer, J. R. Kennedy, J. I. Cole, S. A. Maloy, F. A. Garner, Microstructural analysis of an HT9 fuel assembly duct irradiated in FFTF to 155 dpa at 443 C, J. Nucl. Mater., 393 (2009) 235-241.

74. J. G. Gigax, T. Chen, Hyosim Kim, J. Wang, L.M. Price, E. Aydogan, S. A. Maloy, D. K. Schreiber, M. B. Toloczko, F. A. Garner, L. Shao, Radiation response of alloy T91 at damage levels up to 1000 peak dpa, J. Nucl. Mater. 482, 257-265 (2016).

75. J. G. Gigax, Hyosim Kim, E. Aydogan, S. A. Maloy, F. A. Garner, and Lin Shao, Beam-contamination-induced compositional alteration and its neutron-atypical consequences in ion simulation of neutron-induced void swelling, Mater. Res. Lett. (2017) pp. 1-8.

76. M. P. Short, D. R. Gaston, M. Jin, L. Shao, F. A. Garner, Modelling injected interstitial effects on void swelling in self-ion irradiation experiments, J. Nucl. Mater., 471 (2015) 200-207.

77. G.R. Odette, M.J. Alinger, B.D. Wirth, Recent developments in irradiation-resistant steels, Annu. Rev. Mat. Res. 38, 471-503 (2008).

78. T. Chen, E. Aydogan, J. G. Gigax, D. Chen, J. Wang, X. Wang, S. Ukai, F. A. Garner, and L. Shao, Microstructural changes and void swelling of a 12Cr ODS ferritic-martensitic alloy after high-dpa self-ion irradiation, J. Nucl. Mater., 467 (2015) 42-49.

79. T. Chen, J. G. Gigax, L. Price, D. Chen, S. Ukai, E. Aydogan, S. A. Maloy, F. A. Garner, and L. Shao, Temperature dependent dispersoid stability in ion-irradiated ferritic-martensitic dual-phase oxide-dispersion strengthened alloy: coherent interfaces vs. incoherent interfaces, Acta Mater. 116, 29-42 (2016).

80. E. Getto, K. Sun, A. M. Monterrosa, Z. Jiao, M. J. Hackettc, G. S. Was, Void swelling and microstructure evolution at very high damage level in self-ion irradiated ferritic-martensitic steels, J. Nucl. Mater. 480, 159-176 (2016).

81. X. Wang, Q. Yan, G. S. Was, L. Wang, Void swelling in ferritic-martensitic steels under high dose ion irradiation: exploring possible contributions to swelling resistnance, Scr. Mater. 112, 9-14 (2016).

82. J.J. Kai, R.L. Klueh, Microstructural analysis of neutron-irradiated martensitic steels, J. Nucl. Mater. 230 (2) (1996) 116.

83. J.M. Vitek, R.L. Klueh, Microstructure of 9Cr-1MoVNb steel irradiated to 36 dpa at elevated temperatures in HFIR, J. Nucl. Mater. 122–123 (1984) 254–259.

84. J. Van den Bosch, O. Anderoglu, R. Dickerson, M. Harti, P. Dickerson, J. A. Aguiar, P. Hosemann, M. B. Toloczko, S. A. Maloy, SANS and TEM of ferritic-martensitic steel T91 irradiated in FFTF up to 184 dpa at 413 C, J. Nucl. Mater. 440(2013) 91-97.

85. D.S. Gelles, Microstructural development in reduced activation ferritic alloys irradiated to 200 dpa at 420 C, J. Nucl. Mater. 212–215 (1994) 714–719.

86. C. Wei , A. Aitkaliyeva, M. Martin, D. Chen, L. Shao, Microstructural changes of T91 alloy irradiated by Fe self-ions to ultrahigh displacement ratios, Nucl. Meth. Phys. Res. Sect. B, 307 (2013) 181.

87. V. Bryk, O. Borodin, A. Kalchenko, V. Voyevodin, V. Ageev, A. Nikitina, V. Novikov, V. Inozemtsev, F. A. Garner, Proceedings Accelerator Applications 2013, 5-8 August 2013 Bruges Belgium.

88. K. Thompson, D. Lawrence, D.J. Larson, J.D. Olson, T.F. Kelly, and B. Gorman, In situ site-specific specimen preparation for atom probe tomography, Ultramicroscopy, 107 (2007) 131-139.

89. E. Aydogan, T. Chen, J. Gigax, D. Chen, X. Wang, et al., Effect of self-ion irradiation on the microstructural changes of alloy EK-181 in annealed and severely deformed conditions, J. Nucl. Mater. 487 (2017) 96-104.

90. A. M. Dvoriashin, S. I. Porollo, Yu. V. Konobeev and F. A. Garner, Influence of high dose neutron irradiation on microstructure of EP-450 ferritic-martensitic steel irradiated in three Russian fast reactors, J. Nucl. Mater. 329-333 (2004) 319-323.

91. T. Okita, T. Sato, N. Sekimura, T. Iwai and F. A. Garner, The synergistic influence of temperature and displacement rate on microstructural evolutioin of ion-irradiated Fe-15Cr-16Ni model austenitic alloy, J. Nucl. Mater. 367-370 (2007) 930-934.

92. J. Tenbrink , R.P. Wahi and H. Wollenberger. The swelling of SS AISI 316L under dual beam irradiation as a function of the displacement rate, J. Nucl. Mater. 155-157 (1988) 850-855.

93. J. B. Whitely, G. I. Kulcinski, P. Wilkes, and J. Bullen, The depth dependent damage profile in nickel irradiated with nickel or copper ions, J. Nucl. Mater. 85 & 86 (1979) 701-706.

94. T. Okita, N. Sekimura, T. Sato, F. A. Garner and L. R. Greenwood, The primary origin of dose rate effects on microstructural evolution of austenitic alloys during neutron irradiation, J. Nucl. Mater. 307-311 (2002) 322-326.

95. D. L. Porter and F. A. Garner, Effects of Radiation on Materials: Twelfth International Symposium, ASTM STP 870, F. A. Garner and J. S. Perrin, Eds., ASTM, Philadelphia, PA, 1985, pp. 212-220.

96. Y. E. Kupriiyanova, V. V. Bryk, O. V. Borodin, A. S. Kalchenko, V. N. Voyevodin, G. D. Tolstolutskaya, F. A. Garner, Use of double and triple-ion irradiation to study the influence of high levels of helium and hydrogen on void swelling of 8-12% Cr ferritic-martensitic alloys, J. Nucl. Mater. 468 (2016) 264-273.

97. F. A. Garner, L. Shao, M. B. Toloczko, S. A. Maloy, V. N. Voyevodin, Proc. 17th International Conference on Environmental Degradation of Materials in Nuclear Power Systems – Water Reactors August 9–12, 2015, Ottawa, Ontario, Canada.

98. X. Wang, A.M. Monterrosa, F. Zhang, H. Huang, Q. Yan, Z. Jiao, et al., Void swelling in high dose ion-irradiated reduced activation ferritic-martensitic steels, J. Nucl. Mater. 462 (2015) 119-125.

99. E. Getto, K. Sun, S. Taller, A.M. Monterrosa, Z. Jiao, G.S. Was, Methodology for determining void swelling at very high damage under ion irradiation, J. Nucl. Mater. 477 (2016) 273-279.

100. F. A. Garner, N. I. Budylkin, Yu. V. Konobeev, S. I. Porollo, V. S. Neustroev, V. K. Shamardin, A. V. Kozlov, 11th International Conference on Environmental Degradation of Materials in Nuclear Power Systems – Water Reactors, 2003, pp. 647-656.

101. T. Okita, N. Sekimura, T. Iwai and F. A. Garner, 10th International Conference on Environmental Degradation of Materials in Nuclear Power Systems – Water Reactors, 2001, issued on CD format, no page numbers.

102. V. N. Voyevodin, I. M. Neklyudov, V. V. Bryk, O. V. Borodin, Microstructural evolution and radiation stability of steels and alloys, J. Nucl. Mater 271 & 272 (1999) 290-295.

103. A.S. Kalchenko, V. V. Bryk, N.P. Lazarev, I.M. Neklyudov, V.N. Voyevodin, and F.A. Garner, Prediction of swelling of 18Cr10NiTi austenitic steel over a wide range of displacement rates, J. Nucl. Mater. 399 (2010) 114–121

104. V.A. Pechenkin , A.D. Chernova and, F.A. Garner, Proceedings of Accelerator Applications, 2013, Bruges, Belgium.

105. K. Vörtler, L. Barnard, I. Szlufarska, F. A. Garner, D. Morgan, Simulated spatial and temporal dependence of chromium concentration in pure Fe and Fe-14Cr under high dpa ion irradiation, J. Nucl. Mater. 479 (2016) 23-35.

106. V.K. Sethi and P. R. Okomoto, Proceedings of AIME Symposium on Irradiation Phase Stability, Pittsburgh, PA, (1980), p.109.

107. W. G. Johnston, W.G. Morris and A. M. Turkalo, Proceedings, International Conference on Radiation Effects in Breeder Reactor Structural Materials, Scottsdale, AZ, June 19-23, 1977, p. 509.

108. Todd R. Allen, Djamel Kaoumi, Janelle P. Wharry, Zhijie Jiao, Cem Topbasi, Aaron Kohnert, Leland Barnard, Alicia Certain, Kevin G. Field, Gary S. Was, Dane L. Morgan, Arthur T. Motta, Brian D. Wirth, Y. Yang, J. Mater. Res. 30 (2015) 9.

109. J. G. Gigax, Hyosim Kim, T. Chen, F. A. Garner, L. Shao, Radiation instability of equal channel angular extruded T91 at ultra-high damage levels, Acta Mater. 132 (2017) 395-404.

110. D.C. Foley, K.T. Hartwig, S.A. Maloy, P. Hosemann, X. Zhang, Grain refinement of T91 alloy by equal channel angular pressing, J. Nucl. Mater. 389 (2009) 221-224.

111. C. Sun, S. Zheng, C. C. Wei, Y. Wu, L. Shao, Y. Yang, K. T. Hartwig, S. A. Maloy, S. J. Zinkle, T. R. Allen, H. Wang, X. Zhang, Superior radiation-resistant

nanoengineered austenitic 304L stainless steel for applications in extreme radiation environments, Sci. Rep.5 (2015).

112. X. Sauvage, G. Wilde, S. Divinsky, Z. Horita, R.Z. Valiev, Grain boundaries in ultrafine grained materials processed by severe plastic deformation and related phenomena, Mat. Sci. Eng. A 540 (2012) 1-12.

113. J. Straalsund, Irradiation Creep in Breeder Reactor Materials, in Proceedings International Conference on Radiation effects in Breeder Reactor Structural Materials, Scottsdale, AZ; 1977, p. 191.

114. L. Mansur, Theory and experimental background on dimensional changes in irradiated alloys, J. Nucl. Mater. 216 (1994) 97–123.

115. W. T. Read and W. Shockley, Dislocation models of crystal grain boundaries, Physical Review 78 (1950) 275.

116. F. Humphreys and M. Hatherly, Recrystallization and related annealing phenomena (Pergamon, 1995).

117. M. A. Tschopp, K. N. Solanki, F. Gao, X. Sun, M. A. Khaleel, M. F. Horstemeyer, Probing grain boundary sink strength at the nanoscale: energetics and length scales of vacancy and interstitial absorption by grain boundaries in a-Fe, Phys. Rev. B 85, 064108.

118. D. Chen, J. Wang, T. Chen, L. Shao, Defect annihilation at grain boundaries in alpha-Fe, Sci. Rep. 3 (2013).

119. F.J. Perez-Perez, R. Smith, Modelling radiation effects at grain boundaries in bcc iron, Nucl. Instrum. Methods Phys. Res. Sect. B 164–165 (2000) 487.

120. F.J. Perez-Perez, R. Smith, Structural changes at grain boundaries in bcc iron by atomic collisions, Nucl. Instrum. Methods Phys. Res. Sect. B 180 (2001) 322.

121. X. Bai and B. P. Uberuaga, The influence of grain boundaries on radiation-induced point defect production in materials: a review of atomistic studies, J. Metals 3 (2013) 360-373.

122. B.P. Uberuaga, L. J. Vernon, E. Martinez, and A.F. Voter, The relationship between grain boundary structure, defect mobility, and grain boundary sink efficiency, Sci. Rep. 5 (2015).

123. R.E. Stoller, P.J. Kamenski, and Y.N. Osetsky, Length-scale Effects in Cascade Damage Production in Iron, MRS Proc. 1125 (2008).

124. S. Dey, J. Mardinly, Y. Wang, J. A. Valdez, T. G. Holesinger, B. P. Uberuaga, J. J. Ditto, J. W. Drazin, and R. H. R. Castro, Irradiation-induced grain growth and defect evolution in nanocrystalline zirconia with doped grain boundaries, Phys. Chem. Chem. Phys. 18 (2016) 16921-16929.